

# **The Synthesis and Analysis of Skyrmionic Swedenborgite Materials**

**Bachelor Research Project**

**Tobiáš Halouzka**

Student nr.: s3155110

1.7.2019

First Assessor: Dr. Graeme R. Blake

Second Assessor: prof. Dr. Beatriz Noheda Pinauga

Supervisor: Joshua Levinsky

## 1. ABSTRACT

This research project involved the synthesis of  $\text{CaBaCo}_2\text{Fe}_2\text{O}_7$  and the attempted synthesis of  $\text{CaBaCo}_2\text{V}_2\text{O}_7$  which are both swedenborgite-like compounds. All compounds were made using solid state synthesis and were characterised using powder and single-crystal x-ray diffraction, energy dispersive X-ray spectroscopy (EDS) and magnetization measurements. The  $\text{CaBaCo}_2\text{Fe}_2\text{O}_7$  was determined to belong to the  $P6_3mc$  space group with hexagonal geometry, and the lattice parameters  $a = 6.331 \text{ \AA}$ ,  $b = 6.331 \text{ \AA}$  and  $c = 10.2322 \text{ \AA}$ . The magnetisation was measured at 1T from 300K to 10K and resulted in two ordering peaks at 50K and 140K under zero field. The magnetisation against applied field was measured at 7T at 10K and 100K and showed hysteresis at both temperatures. The magnetization measurements showed ferromagnetic and antiferromagnetic ordering in  $\text{CaBaFe}_2\text{Co}_2\text{O}_7$ . The crystal growth of  $\text{CaBaCo}_2\text{V}_2\text{O}_7$  resulted in oxidation of the vanadium, and the formation of barium vanadate ( $R\bar{3}$  space group, rhombohedral) single crystals. The crystal growth was carried out again using a 37%:63% mixture of  $\text{CaCl}_2$  and  $\text{BaCl}_2$  as flux, which reacted with the compound to make  $\text{Co}_3\text{O}_4$  and  $\text{Ca}_2(\text{VO}_4)\text{Cl}$  (orthorhombic). Using  $\text{CaCl}_2$  as a flux by itself resulted in the formation of a monoclinic unidentified crystal compound with point group  $P2_1c$ .

## 2. INTRODUCTION & THEORY

Magnetic Skyrmions are configurations of a local cluster of magnetic moments with particle-like behaviour. They are topologically protected structures that can be formed using a variety of mechanisms, either in bulk or on thin films<sup>1,2</sup>. Descriptions of skyrmions include discussion on topology – properties of space stay preserved under deformation. These descriptions specify a non-zero integer, which is commonly referred to as the Topological Skyrmion Number ( $N_{skyr}$ )<sup>3</sup>,

$$N_{skyr} = \frac{1}{4\pi} \int d^2r n \times \left( \frac{\partial n}{\partial x} \times \frac{\partial n}{\partial y} \right) = \pm 1 \quad (\text{eq.1})$$

where  $n = M/|M|$ , which is the unit vector in the magnetisation direction. The skyrmion number can equal to +1, which means that the spin structure is a skyrmion, or -1, which indicates an anti-skyrmion. Skyrmions also possess an additional property called helicity, which determines the chirality of the skyrmion. The chirality creates interactions between spins and combining this with the crystal symmetry of the material determines the method of skyrmion formation, and also the type of skyrmion formed. There are four known mechanisms that lead to skyrmion formation.

The first formation mechanism is the competition between the Dzyaloshinskii-Moriya (DMI) and ferromagnetic exchange interaction. The DMI is an asymmetric spin interaction which is caused by strong spin-orbit coupling<sup>4</sup>. It favours a rotating magnetisation alignment with a ninety degree turn angle. It competes with ferromagnetic exchange interaction, and that favours a collinear ferromagnetic spin alignment<sup>5</sup>. The competition of these interactions results in a helical structure, with a uniform, periodic turn angle, which leads to the spiral shape that is characteristic of skyrmions. Skyrmions form in a hexagonal lattice, to create skyrmion crystals, which then stack to form rods using ferromagnetic interactions. The size of the skyrmions is determined by the ratio of the Dzyaloshinskii-Moriya Interaction to the ferromagnetic exchange integral (D:J) and is in the range of 3–100 nm<sup>6</sup>.

The second mechanism occurs in thin-films of ferromagnets and is caused by a competition between long range magnetic dipolar interactions and the perpendicular easy-axis anisotropy<sup>7</sup>. In this interaction, the dipolar interactions favour in-plane magnetizations and the anisotropy favours out-of-plane magnetizations. This competition results in a stripe with rotating spins in a thin film plane, with a periodic rotation. When a magnetic field is applied perpendicular to the film, the rotating spins arrange into a vortex, forming a skyrmion. Using this method, the skyrmions that are formed are much

larger (100 nm - 1 $\mu$ m) than that of the first mechanism<sup>8</sup>. The DMI interaction is not applied here, the skyrmions have an extra degree of freedom, which is the helicity. This means that both skyrmions have the same energy and both can be observed.

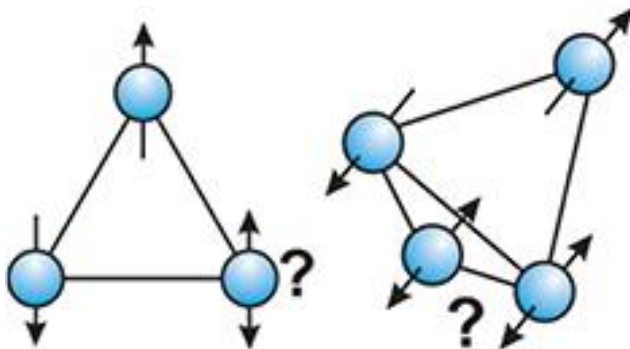


*Figure 1: Geometric frustration in triangular and tetrahedral lattices of antiferromagnetic materials (Source: Woznitsa et al.<sup>11</sup>)*

The third mechanism is caused by geometrically frustrated antiferromagnets<sup>9</sup>. Geometric frustration can be used (in theory) to produce skyrmions in a triangular lattice. In an antiferromagnet, the adjacent spins are aligned oppositely with respect to each other. In a triangular lattice, multiple ground states can be available to the system if only two of the spins are coupled. However, the third spin is coupled to both, and can be either spin-up or spin-down. To overcome this “frustration”, the spins orientate themselves in a way so that they are at an angle of 120° to each other. This angular tilt could be the source of the

skyrmion formation<sup>10</sup>. This theory was the basis of the choice of materials to be examined in this project, as the swedenborgites used are known to be antiferromagnetic. In theory, the size of the skyrmions made using this method should be the same as the order of the lattice constant (approx. 1 nm<sup>8</sup>).

The last known mechanism to generate skyrmions is through competition between the four-spin exchange interaction and the aforementioned Dzyaloshinskii-Moriya interaction. The DMI can stabilize the skyrmion spin texture in non-centrosymmetric materials, but also in materials where the inversion symmetry is broken. This mechanism has been found to generate a skyrmion square lattice on a hexagonal iron layer on Ir(111).<sup>3</sup> The four-spin interaction is the interaction between four adjacent spins which results from electrons moving between four spin sites which are all next to each other. The two interactions that are part of this mechanism are competing with each other – the four-spin exchange enforces the square the lattice and is the driving force of skyrmion formation. The DMI interaction simply determines the helicity of the skyrmion, i.e. it determines if the skyrmion formed will be a skyrmion or an antiskyrmion. The size of the skyrmions formed through this mechanism is on the scale of 1 nm<sup>11</sup>.

In this project, a group of materials called “swedenborgites” was synthesized and tested for skyrmionic behaviour. Swedenborgites are a group of metal oxides, which are structurally based on the compound called Swedenborgite (NaSbBe<sub>4</sub>O<sub>7</sub>)<sup>12</sup>. They have become widely used in the scientific community for their magnetic and electric properties. Up until recent years, it has been thought that the only materials that exhibit skyrmionic behaviour are chiral magnets<sup>13</sup>. However, it has been assumed that swedenborgites can display skyrmionic behaviour due to the interactions that take place in the material – namely, the DMI and antiferromagnetic frustration.

There are a number of methods that are used to detect and confirm skyrmionic behaviour in magnetic materials. Firstly, to get a hint (but not a confirmation) of skyrmion structures, the MPMS (Magnetic Property Measurement System) could be used. It is a magnetometer that uses a liquid helium cooled SQUID (Superconducting Quantum Interference Device) which measures magnetization as a function of temperature or applied magnetic field. The presence of skyrmions in a material would show up as an anomaly in the measurement, however the smallest amount of impurities could trigger such an

anomalous result. This method would be used as it is more economical to use over the other, more direct methods described below.

To investigate the skyrmion structure, there are multiple available techniques. Small-Angle Neutron Scattering (SANS) can be used. It is preferred over X-Ray scattering, as using neutrons can show the presence of localized magnetic fields, due to the strong scattering by magnetic moments. Pfleider et al.<sup>1</sup> have used this method to show the formation of a skyrmion lattice in bulk MnSi. In all of their results, all scattering patterns showed a six-fold symmetry, suggesting the formation of a skyrmion lattice.

To get a real-space image of the skyrmion lattice, Lorentz Transmission Electron Microscopy (LTEM) can be used. This analysis technique uses an electron beam which is emitted at the sample. As it passes through the magnetic sample, each electron changes its direction of propagation due to the Lorentz Force that comes from the magnetizations of the sample. The Lorentz Force is the force that is exerted on the electron moving with a certain velocity as it passes through an electric and magnetic field. Due to the change in direction, we can take over-focused and under-focused images, which we can use to obtain the real space distribution of magnetic moments in our sample<sup>15</sup>.

### 3. EXPERIMENTAL

The target compounds were synthesized using a solid-state reaction of the starting compounds in stoichiometric amounts ( $\text{CaCO}_3$ ,  $\text{BaCO}_3$ ,  $\text{Fe}_2\text{O}_3$ ,  $\text{Co}_3\text{O}_4$  and  $\text{V}_2\text{O}_3$ ). These powders were dried in an alumina crucible for 2-3 hours at  $600^\circ\text{C}$ , before being thoroughly mixed in an agate mortar until the colour of the mixture became homogeneous. For  $\text{CaBaCo}_2\text{Fe}_2\text{O}_7$  the mixed sample was rusty brown, due to the presence of the dark black cobalt oxide and the red iron oxide. For  $\text{CaBaCo}_2\text{V}_2\text{O}_7$ , the vanadium oxide resulted in a dark green mixture, though it must be noted that the vanadium oxide was very impure judging by its colour, as it is supposed to be black rather than green. The mixtures were then heated in a furnace in alumina and platinum crucibles, using different heating profiles – heating to  $1000\text{-}1100^\circ\text{C}$  at  $5^\circ\text{C}/\text{min}$  for 2 to 12 hours, and then heating at  $900^\circ\text{C}$  overnight. After the heat treatment, all samples were ground again using the agate mortar. Some of the samples were then heat-treated again using the same heating profiles. All samples were analysed with powder XRD (Bruker D8 Advance,  $\text{Cu-K}\alpha_1$  radiation,  $\lambda=1.54051 \text{ \AA}$ ) after each heat treatment to identify any present impurities.

After heat treatment,  $\text{CaBaCo}_2\text{Fe}_2\text{O}_7$  single crystals were formed in the alumina crucibles by heating rapidly to  $1200^\circ\text{C}$  ( $40^\circ\text{C}/\text{min}$ ) for 30 minutes, and then cooling slowly to room temperature. The cooling times were varied between 4 hours and 55 hours. This process had caused the sample to compact into a coin shape, with the single crystals forming around the edge of the sample, as well as the edge of the crucible. The crystals were then mechanically removed and examined under a microscope. For the vanadium-based compound, the same method as well as a flux was used for crystal growth. The fluxes that were used for this method were calcium chloride, barium chloride, and a 37% : 63% mixture of both. The weight ratio of the flux to sample used in each case was 8:1. Since the melting points of each of the fluxes have a large temperature difference between each other<sup>17</sup>, the temperatures used in the experiment were much higher than necessary ( $950\text{-}1050^\circ\text{C}$  instead of  $600\text{-}900^\circ\text{C}$ ) due to a temperature difference limitation from the furnace that was used. The compounds were cooled for approximately 96 hours. The experiment was also performed in a tube furnace under an argon atmosphere, to prevent any unwanted oxidation of vanadium. The resulting crystals were removed from the flux by dissolving the soluble flux compounds in water, which were

then decanted. A small amount of acetone was then added to the crystals, and was let to evaporate, which left the crystals dry.

The single crystals of each sample were analysed using Single Crystal XRD (Bruker D8 Venture, Mo-K $\alpha_1$  radiation,  $\lambda=0.7107 \text{ \AA}$ ). The powder XRD sets of data were analysed using Jana2006<sup>18</sup> and single crystal XRD data was analysed with Bruker APEX 3 software for refinement.

Analysis of magnetic properties was done by the MPMS XL 7T SQUID magnetometer. Three different types of sample were used in analysis: single crystal, single crystal stack with the same orientation, and powder made from single-crystalline material. The lattermost gave the only reliable signal. As for the other two attempts, the signal was too weak, the sample was too impure, or the data was unreliable due to technical issues with the instrument. The magnetic susceptibility of the sample was measured using zero-field cooling from 300K to 10K and field cooling using the same temperature range and a field of 1T. The M-H curve was measured at 7T at temperatures of 10K and 100K.

The size of the single crystal and their composition was analysed using scanning electron microscopy (SEM) and energy dispersive X-ray spectroscopy (EDS). A collection of single crystals was coated with a 10 nm thick layer of gold. A voltage of 18 kV and a spot size of 5.0 mm was used for the analysis.

## 4. RESULTS AND DISCUSSION

### 4.1 SYNTHESIS

(The list of analysed samples and their details can be found in Appendix A: Table 10.) When using the alumina crucible at 1100°C for longer periods of time, it was found that the cobalt oxide had stained the lower sides of the crucible with a deep blue colour. This is due to the reaction between cobalt oxide and the crucible, forming cobalt aluminate (confirmed by PXRD), also known as Cobalt Blue. This reaction was limited when the temperature was reduced to 1000°C and completely eliminated when using the platinum crucible due to the metal's inert properties. This side reaction has already been briefly mentioned by Valldor<sup>16</sup>.

After heat treatment of every sample, it was observed that the powder had been compacted and had shrunk towards the centre of the crucible. This is due to the elimination of carbon dioxide from each of the carbonate precursors, and also the formation of the overall crystal structure, which has shorter bond lengths compared to the interatomic distance between the metal atoms of two different starting materials. The samples that were heated for a second time became more dense, as their grain boundaries fused together.

A significant colour change was observed for all samples – the compound containing cobalt had now turned completely black (including some blue from the side reaction) and the vanadium compound had also turned black, until it was ground with the mortar where the sample turned dark green, suggesting that the sample had oxidized.

In all cases, every sample crystallised in the same manner and into hexagonal single crystals. Most of the sample solidified into a coin shape made of amorphous material, and the single crystals formed around the edge of the “coin” as well as the inner edge of the base of the crucible. In growing crystals, the longest cooling time should result in the biggest crystals. This was not the case in this experiment. The 21-hour cooling gave far better results than the 55-hour cooling. For the 4-hour cooled sample, the single crystals only formed around the inner edge of the crucible and a very small portion of the amorphous sample. For the 21-hour cooled sample, the single crystals were much larger, and formed

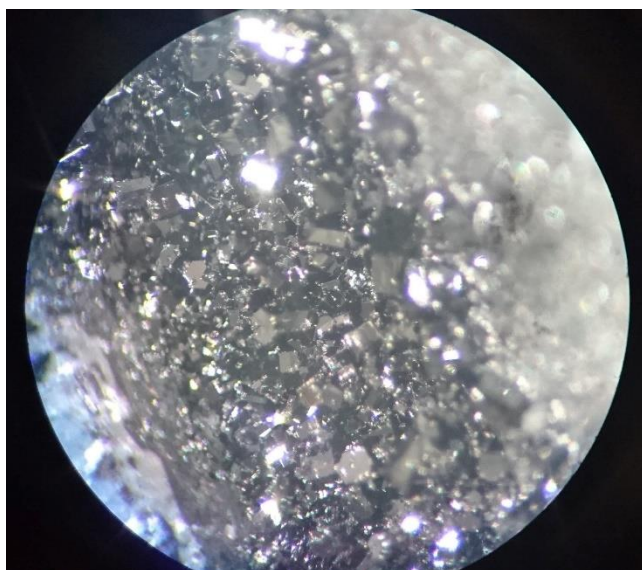


*Figure 2: Single crystals of CaBaCo<sub>2</sub>Fe<sub>2</sub>O<sub>7</sub> under a microscope (cooled for 21hrs)*

all around the amorphous sample, as well as the inside of the crucible. For the 55-hour cooling, the crystals formed on the edge of the sample, but only in small amounts and in smaller dimensions than for the previous two samples. Some large crystals did appear on the inside of the crucible, however they appeared dull and were impossible to remove without being destroyed. On the other hand, the single crystals of the other two samples were very shiny, to the point where their reflection could be easily visible with the naked eye. The reason for the localised crystallization is most likely due to better thermal insulation at the edges of the crucible than at the centre of its base. But the reason for the worse crystallization at the slowest

cooling rate is difficult to explain. Nucleation may have been prevented due to a differing level of impurities, or maybe the sample used was not a homogeneous mixture.

The platinum crucible was not suitable for crystal growth. The used crucible had a structural irregularity at its base, which was hoped to serve as a nucleation point for crystal growth. However, single crystals did not form at all, and the sample was impossible to remove without being damaged.

The crystallization attempt of Sample 12 was carried out in a box furnace exposed to the atmosphere. After the sample had fully cooled to room temperature, there were three distinct phases formed: Amorphous dark crystals, amorphous purple crystals, and plate-like transparent crystals. The first two crystal types were not identified, but it is assumed due to their colour that the first contained cobalt and the second contained an oxidised form of vanadium, possibly vanadium(IV). Again, the upper walls of the crucible were stained blue due to the formation of cobalt aluminate.

The flux growth attempt resulted in crystals from the two fluxes as well as the mixed flux. After drying, there were two distinct compounds in the mixed flux sample – transparent block-like crystals and crystalline black flakes, with octahedral single crystals growing on their edges. Both were analysed using single crystal XRD. The octahedral crystals were truncated, and so they appeared as hexagonal crystals through the optical microscope. The octahedral structure was only observable when examining the sample under the electron microscope.

## 4.2 POWDER X-RAY DIFFRACTION

(The results of the PXRD can be found in Appendix B: Figures 17-20.) The geometry and space group of CaBaFe<sub>2</sub>Co<sub>2</sub>O<sub>7</sub> were determined using PXRD. All of the samples that were tested using PXRD gave the same result for geometry and space group, namely hexagonal geometry, with  $P6_3mc$  space group. This can further be confirmed in the paper by Valldor<sup>16</sup>. PXRD was also used to analyse the effect of the different parameters in the synthesis – the total heating time of the samples, the temperature and the choice of crucible.

The results of PXRD analysis of sample 1 already allowed for some tweaking of the synthesis procedure. Apart from identifying the main phase of the product, other phases were also identified.

One of these phases was already observed during the synthesis, due to its strong blue colour. This was confirmed to be  $\text{CoAl}_2\text{O}_4$  and it improved the fitting factor. The aluminates of iron(II) and barium were also identified and also they both improved the fitting factor. Out of the starting compounds, only the cobalt(II, III) oxide was observed. From this we can conclude that the cobalt oxide did not fully react due to its volatile behaviour at high temperatures, which also explains the formation of cobalt aluminate along the walls of the crucible. The same sample was then tested again after a second day of heat treatment (Sample 2). The results were similar in that they showed the  $\text{Co}_3\text{O}_4$  and  $\text{CoAl}_2\text{O}_4$  phases, as well as each of the metal aluminates, as from the analysis of Sample 1. It is probable that more of the aluminates formed in sample 2, due to its longer heat treatment. The reaction temperature used in this method was most likely too high, since some of these aluminates have been reported to form at lower temperatures, using the same method<sup>19</sup>. Due to the presence of  $\text{Co}_3\text{O}_4$  in the second sample, we can deduce that an extra day of heat treatment during synthesis is still not long enough to eliminate all of the starting precursors from the initial mixture.

Due to the high amounts of aluminates forming in the product, all following syntheses using the alumina crucibles were carried out at  $1000^\circ\text{C}$ . Sample 3 appears to be less pure than the samples 1 or 2. Upon analysis we can see that aluminates are still forming, and the same starting products are still visible. This reduction in reaction temperature may have decreased the amount of cobalt aluminate forming along the sides of the crucible, however it is still detected in the PXRD spectrum. Therefore, we can say that the lower temperature has decreased the formation of metal aluminates but has not fully eliminated them.

In order to eliminate the presence of aluminates in the final product, the source of aluminate must be removed. Sample 8 was synthesized in a platinum crucible, in hopes that a purer PXRD spectrum would be obtained. The PXRD spectrum showed the presence of the starting compounds, even though the temperature was raised to  $1100^\circ\text{C}$ . The contribution of the starting materials is lower for sample 8 (and as a result, sample 9) than for the samples made in alumina crucibles, which means that the reaction got closer to completion in sample 8. In sample 9, there was a lower contribution of cobalt aluminate than in previously synthesised samples, however the other aluminates present gave a higher contribution.

The space group of Samples 11 & 12 was determined using PXRD to be  $P3_1c$ . Similar to the iron-based compound, the main impurities found were cobalt oxide and metal aluminates. Also, the second day of heating (Sample 12) caused more of the impurities to form. The heating under a reducing hydrogen/argon atmosphere limited the oxidation, as there was no colour change visible after the heating.

### 4.3 SINGLE CRYSTAL X-RAY DIFFRACTION

Single crystal XRD was used to find the crystal structure of the samples. A single crystal of approximately 0.2 mm width was used from Sample 7 for the  $\text{CaBaFe}_2\text{Co}_2\text{O}_7$  compound. The geometry and crystal structure of the compound as analysed by SCXRD is shown in Table 1.

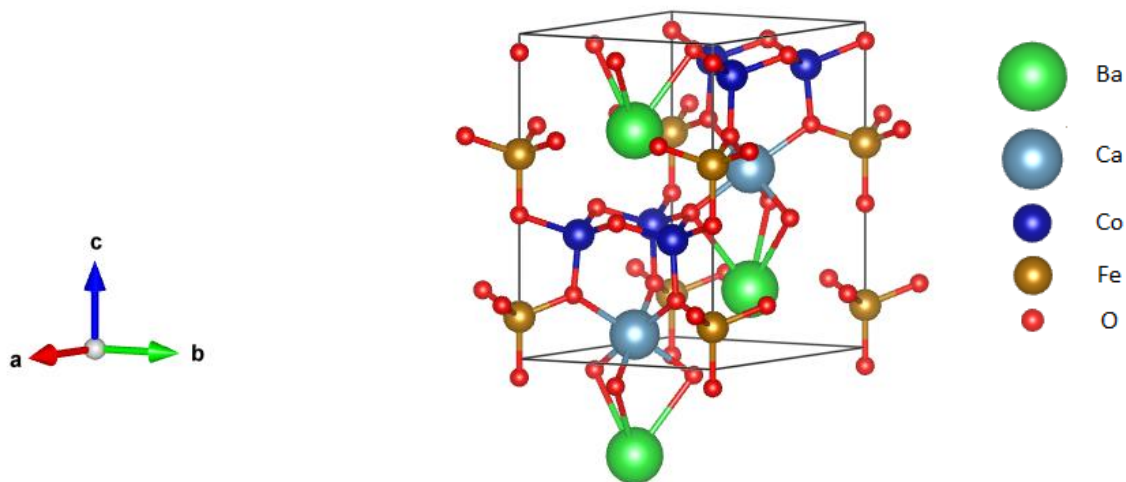


*Figure 3: Crystal structure of a unit cell of  $\text{CaBaFe}_2\text{Co}_2\text{O}_7$  taken using VESTA (Visualisation for Electronic and Structural Analysis)*

A total of 1349 reflections were measured, with a goodness of fit equal to 1.208,  $R1 = 0.0508$  and  $R2 = 0.0537$ . From these figures we can see that the calculated intensities match quite well with those of the measured reflections. Using the data in Table 1, we can also confirm the validity of the geometry data that was received from powder XRD on the same compound.

Space Group	$P6_3mc$
a	6.331(4) Å
b	6.331(4) Å
c	10.2322(7) Å
$\alpha$	90.00°
$\beta$	90.00°
$\gamma$	120.00°
Geometry	Hexagonal
Volume	355.1765 Å <sup>3</sup>

*Table 1: Geometry of  $\text{CaBaFe}_2\text{Co}_2\text{O}_7$  analysed using Single Crystal XRD.*

The crystal structure consists of two alternating layers. The first layer is a tetrahedral  $\text{BaO}_3$  structure, adjacent to three triangularly connected tetrahedral  $\text{CoO}_4$  structures. The second layer consists of four separated  $\text{FeO}_4$  tetrahedra, along with an  $\text{CaO}_6$  octahedron, which connects to the cobalt oxide polyhedra, three of the iron oxide polyhedra, and the barium oxide polyhedron of the lower layer. The polyhedral structure of the compound is shown in Figure 4.

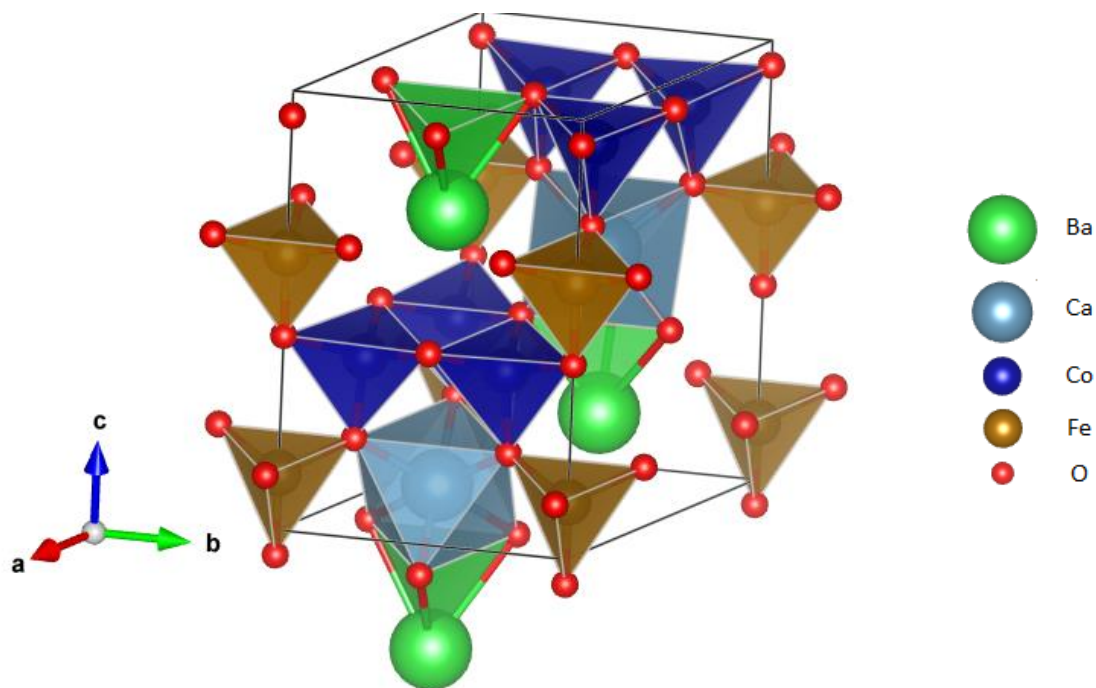


Figure 4: Polyhedral perspective of the  $\text{CaBaCo}_2\text{Fe}_2\text{O}_7$  structure

All of the oxygen atoms act as bridges between each metal atom, suggesting that superexchange may be present, in particular along the Co-O-Fe bonds. The bond lengths are displayed in Table 2. There are multiple values for each type of bond, as the bond length is affected also by the other atom that is attached to the oxygen in question.

Bond	Lengths (Å)
Ba-O	3.1041(161), 3.1675(3)
Ca-O	2.3037(74), 2.3439(68)
Fe-O	1.8257(62), 1.9112(103)
Co-O	1.8699(40), 1.8894(83), 2.0053(36)

Table 2: Bond lengths of  $\text{CaBaCo}_2\text{Fe}_2\text{O}_7$

This structure seems to match that of the compound that was reported by Valldor<sup>16</sup>, the only major difference being in the fact that the bonds are between different atoms. When the structure is viewed from the  $c$  axis, we can see the hexagonal pattern of the Kagomé lattice. (Figure 5)

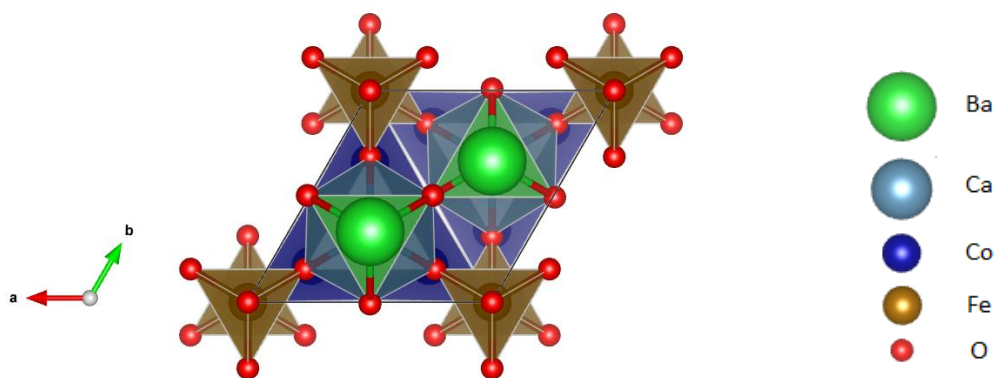


Figure 5:  $\text{CaBaCo}_2\text{Fe}_2\text{O}_7$  structure viewed along  $c$ -axis

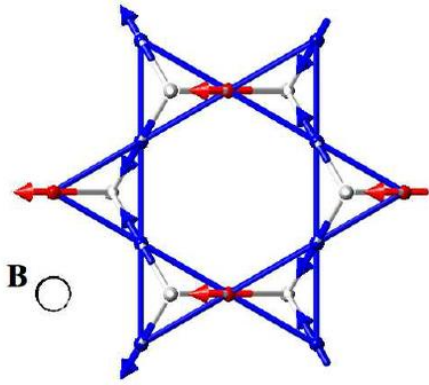


Figure 6: Kagomé Lattice with frustrated spins (from Macdonald et al.<sup>25</sup>)

In Figure 7 is the precession image of the  $OkI$  reciprocal planes of the sample. According to the reflection conditions of the  $P6_3mc$  space group, in all  $00l$  and  $hhl$  planes, the  $l$  values must equal  $2n$ . This rule holds, because if the central vertical line is inspected, we can see that every second spot is missing. These missing spots correspond to the odd-numbered planes, i.e.  $001$ ,  $003$ ,  $005$  etc. However, even though they are allowed to be visible, the  $008$  and  $0014$  reflections are not visible. The reason for this is that their intensities are very low by coincidence, and therefore cannot be seen above the background intensity. Since these reflections follow the conditions of the space group, we can confirm the validity of the powder XRD results. The other precession images can be found in Appendix C: Figures 21-25.

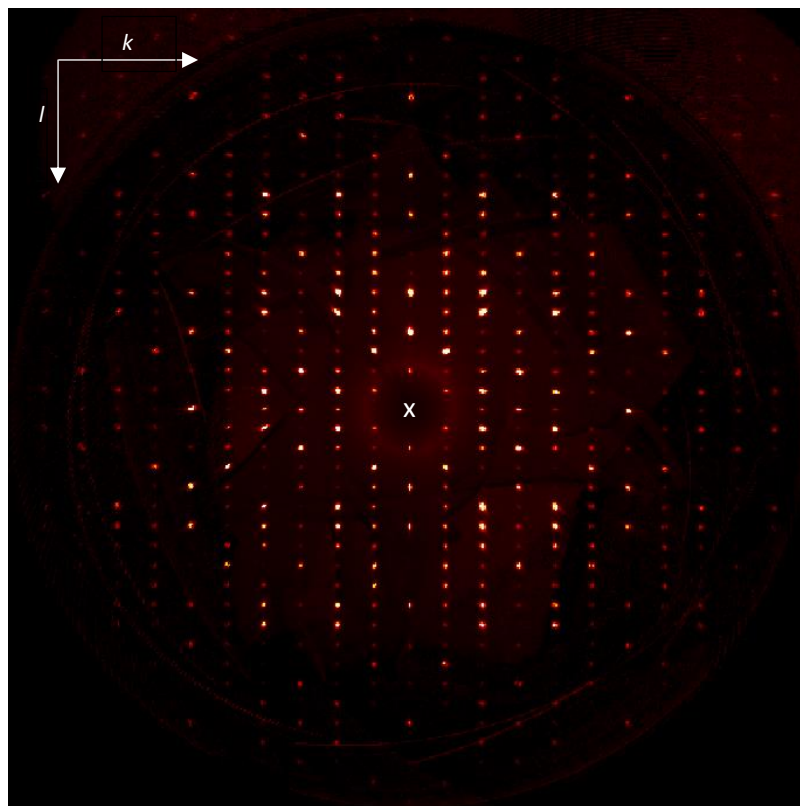


Figure 7:  $OkI$  Precession image of a  $\text{CaBaCo}_2\text{Fe}_2\text{O}_7$  single crystal ( $k=0$ ,  $l=0$  marked by white "x")

The single crystal XRD analysis was carried out on the transparent crystals from Sample 13. On observation, the crystals appeared to have a hexagonal geometry. The compound was found to be barium vanadate –  $\text{Ba}_3(\text{VO}_4)_2$ . This was confirmed by matching the reported cell parameters and the calculated space group to what was reported in literature (see Table 3).

Term	Experimental Result	Reported Result (from Süsse et. al <sup>20</sup> )
<i>a</i>	5.7634(7) Å	5.762(8) Å
<i>b</i>	5.7634(7) Å	5.762(8) Å
<i>c</i>	21.2963(28) Å	21.29(3) Å
$\alpha, \beta, \gamma$	90°, 90°, 120°	90°, 90°, 120°
Space group	R-3	R32 or R3m or R-32/m

**Table 3:** Cell Parameters and Space Group of Barium Vanadate (Sample 13)

The method of flux growth was far more successful in growing crystals than the previously used method of simply heating and slowly cooling the sample. In the case of the mixed flux and the barium chloride flux growth, both resulted in the same crystals. The dark octahedral crystals were found to be  $\text{Co}_3\text{O}_4$  and the block-like transparent crystals were found to be a compound called calcium vanadate chloride -  $\text{Ca}_2(\text{VO}_4)\text{Cl}$ . Similar to the case of Sample 13, the presence of the two compounds were confirmed by comparisons of the crystals geometry to previously reported figures. The cell parameters and geometry of both compounds are listed in Tables 4&5.

Term	Experimental Result	Reported Result (from Banks et. al <sup>21</sup> )
<i>a</i>	6.3 Å	6.311(5) Å
<i>b</i>	7.15 Å	7.140(5) Å
<i>c</i>	11.08 Å	11.052(5) Å
$\alpha, \beta, \gamma$	90°, 90°, 90°	90°, 90°, 90°
Crystal Type	Orthorhombic	Orthorhombic

**Table 4:** Cell Parameters and Crystal Type of Calcium Vanadate Chloride (Sample 17a+c)

Term	Experimental Result	Reported Result (from Roth et. al <sup>22</sup> )
<i>a</i>	8.08 Å	8.084 Å
<i>b</i>	8.08 Å	8.084 Å
<i>c</i>	8.08 Å	8.084 Å
$\alpha, \beta, \gamma$	90°, 90°, 90°	90°, 90°, 90°
Crystal Type	Cubic	Cubic

**Table 5:** Cell Parameters and Crystal Type of Cobalt (II, III) Oxide (Sample 17a+c)

The results of the calcium chloride flux growth were different, however. Firstly, the crystal structure that was calculated was not orthorhombic, but monoclinic, and as a result, different cell parameters were calculated. See Table 6 for the cell parameters and geometry of this compound. Unfortunately, solving the crystal structure was unsuccessful as the structure with the best fit did not make any sense, as the bonds were abnormally long, and some weren't even physically possible. When the structure was changed to something that was physically possible, it made the fit much worse.

Term	Experimental Result
<i>a</i>	6.68 Å
<i>b</i>	10.86 Å
<i>c</i>	7.11 Å
$\alpha, \beta, \gamma$	90°, 91.22°, 90°
Crystal Type	Monoclinic
Space Group	P2 <sub>1</sub> C

**Table 6:** Measured Values of Sample 17b (unidentified)

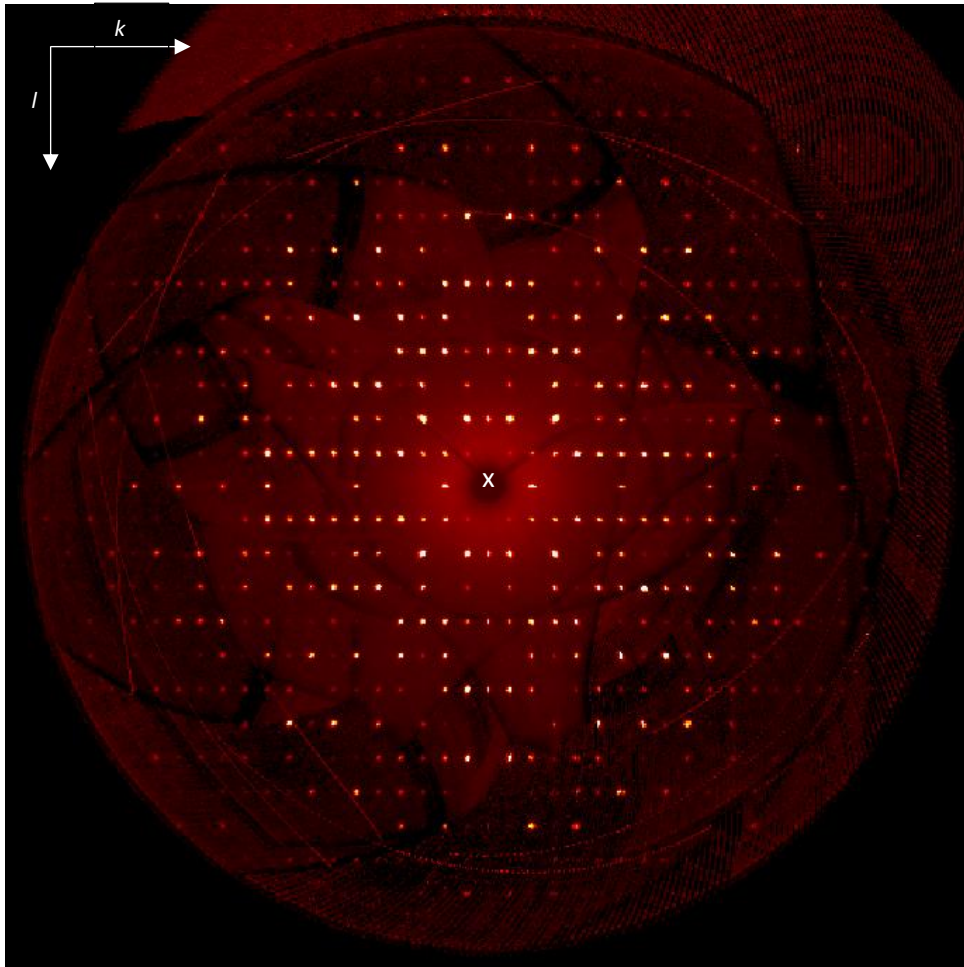


**Figure 8:** Precession image of a  $0kl$  plane of the unidentified compound in Sample 17b ( $k=0, l=0$  marked by white "x")

Similar to that of Sample 7, the precession images of Sample 17b (Figure 8) had missing spots, even though they should be visible. Again, this is most likely because the intensity of the spots is too low to be distinguished from the background. The point group of the unidentified compound is  $P2_1c$ , and according to the reflection conditions, in all  $h0l$  and  $00l$ ,  $l = 2n$ . Similarly, in all  $0k0$  planes,  $k = 2n$ . In Figure 8 we can see that the periodicity along the  $0k0$  direction, where only the even-numbered spots are clearly visible, however the  $040$  and  $080$  spots are missing. The same happens in the same image for  $008$ , and  $0012$ . The rest of the precession images for the sample are found in Appendix C: Figures 26-30.

#### 4.4 MAGNETIC PROPERTIES

The sample of  $\text{CaBaFe}_2\text{Co}_2\text{O}_7$  was first cooled in zero field from 300K to 10K, then a field of 1 T was applied, and the sample was measured on warming back to 300K. After the initial temperature was reached, the sample was cooled in the presence of the same field down to the same temperature and the data were again collected on warming. The results are shown in Figure 9.

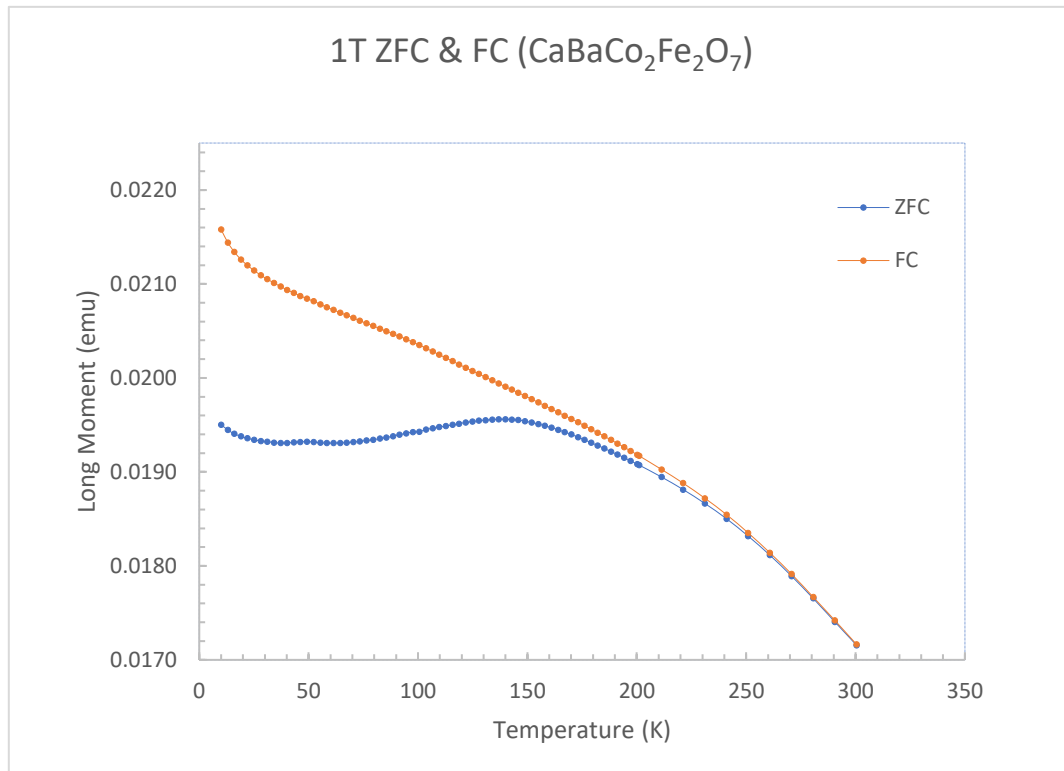


*Figure 9: Magnetisation curve of field cooled (1T) and zero-field cooled  $\text{CaBaCo}_2\text{Fe}_2\text{O}_7$*

The zero-field curve shows a broad peak at 140K and another small peak at 50K. Both curves above 200K show ferromagnetic behaviour, as they appear to be approaching a value  $T_c$  which is outside the boundaries of this graph. Below 140K under zero field, we can see antiferromagnetic behaviour, but not completely, as above this temperature the curve doesn't follow the Curie-Weiss Law. The second smaller peak at 50K may be a result of a magnetic phase transition, however from the above data it is impossible to say what transition it is. The reason for the divergence of the two lines below 200K is because when the field is applied, it can force more of the magnetic moments to point towards the direction of the field, which gives a larger overall magnetic moment. According to Reim et. al.<sup>23</sup>, this material behaves paramagnetically after 750K, after which the Curie-Weiss behaviour can be seen. The data in Fig.6 is close to the data reported by Reim et al., as they measured ordering at 159K, although their sample was measured at 0.1 T. They also observed a small peak at 60K, stating that it was most likely due to spin reorientation, where the spins are flopped out of the Kagomé layers as the sample was cooled<sup>23</sup>.

The magnetisation against applied field was measured at 10K and 100K at a 7T field. For both temperatures, hysteresis is observed (Figure 10).

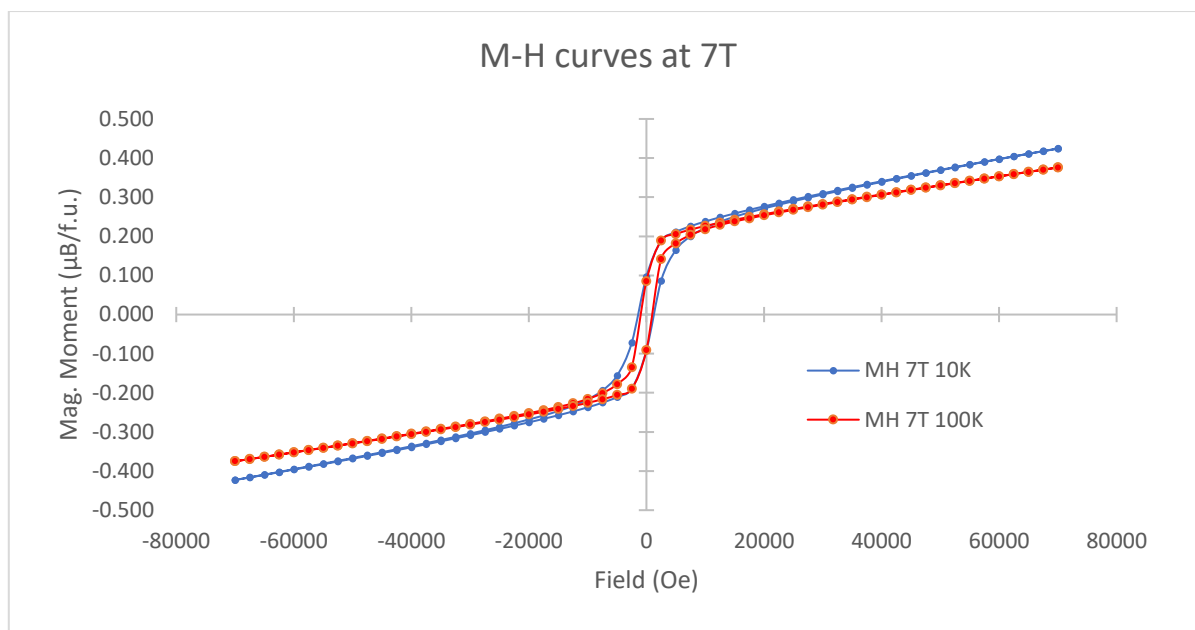


*Figure 10: M-H Curves at 7T (10K and 100K)*

The hysteresis loops confirm that the tested sample exhibits ferromagnetic behaviour. However, the sample has not reached magnetic saturation in the tested conditions, as the curves do not level off to a maximum M value. It is unclear whether the induced magnetic moment comes from the magnetic sample or from a magnetic impurity, because the magnetic moment is too high to come from an impurity and too low to be purely from the magnetic compound. The reason for the divergence of the two data lines at the extremes of the applied field may be due to some ferrimagnetic behaviour. The remanence from the ferromagnetic component is approximately 0.2 Bohr magnetons per formula unit. Comparing the value to that of Reim et al.<sup>23</sup>, we can see that the ferromagnetic interaction in the sample is stronger than what they tested, as their value for remanence is very small ( $\sim 0.001 \mu_B/f.u.$ ). The coercive field of the compound is approximately 1000 Oe.

To confirm that the dark octahedral crystals in samples 17a & 17c were cobalt (II, II) oxide, its magnetic properties were tested. Approximately 1 mg of the powdered single crystals were used for the measurements (Figure 11). The same method for measuring the long moment as a function of temperature from Figure 9 was used.

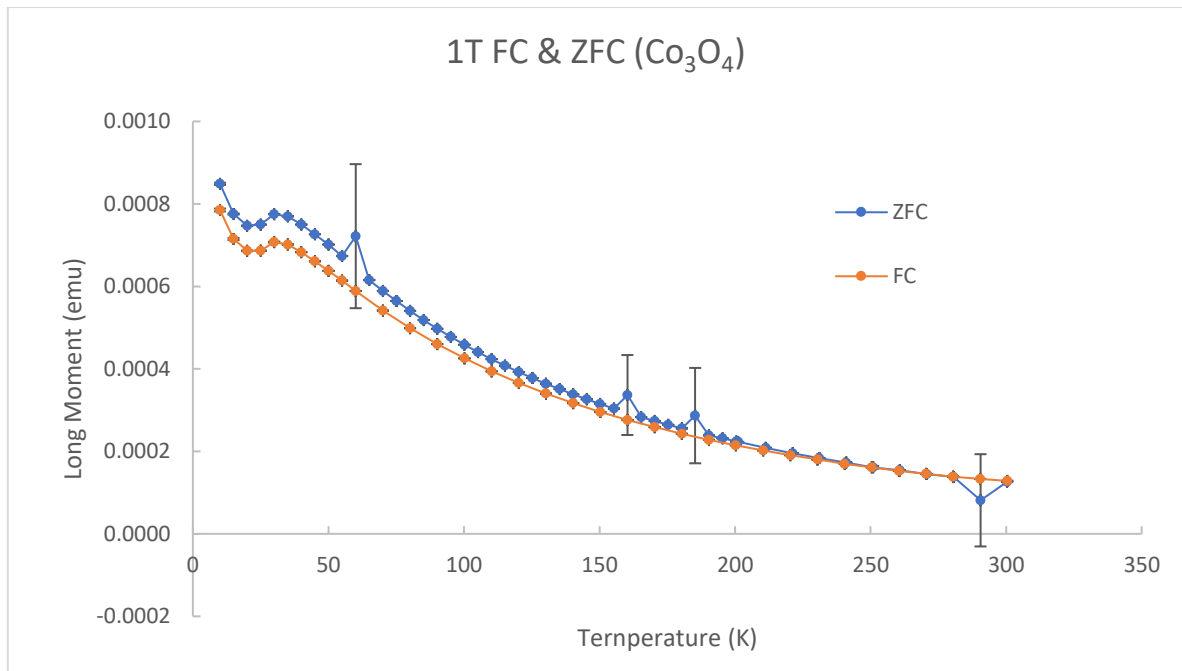


**Figure 11:** Magnetisation curve of field cooled (1T) and zero-field cooled  $\text{Co}_3\text{O}_4$

The graph shows that the curves obey the Curie-Weiss Law, as there is a peak at approximately 35K, indicating an ordering, and both curves level off as the temperature increases. This ordering temperature is in agreement with what was found by He et al. (33K – 39K)<sup>24</sup>. For the zero-field cooled measurement, there are a few data points that are offset from the curve, however they are not reliable, due to the very high standard deviation values marked by the error bars on the graph.

The magnetisation of the same sample was measured at 10K under a 5T field. The measurement is shown in Figure 12 and shows an approximately linear relation between applied field and magnetisation.

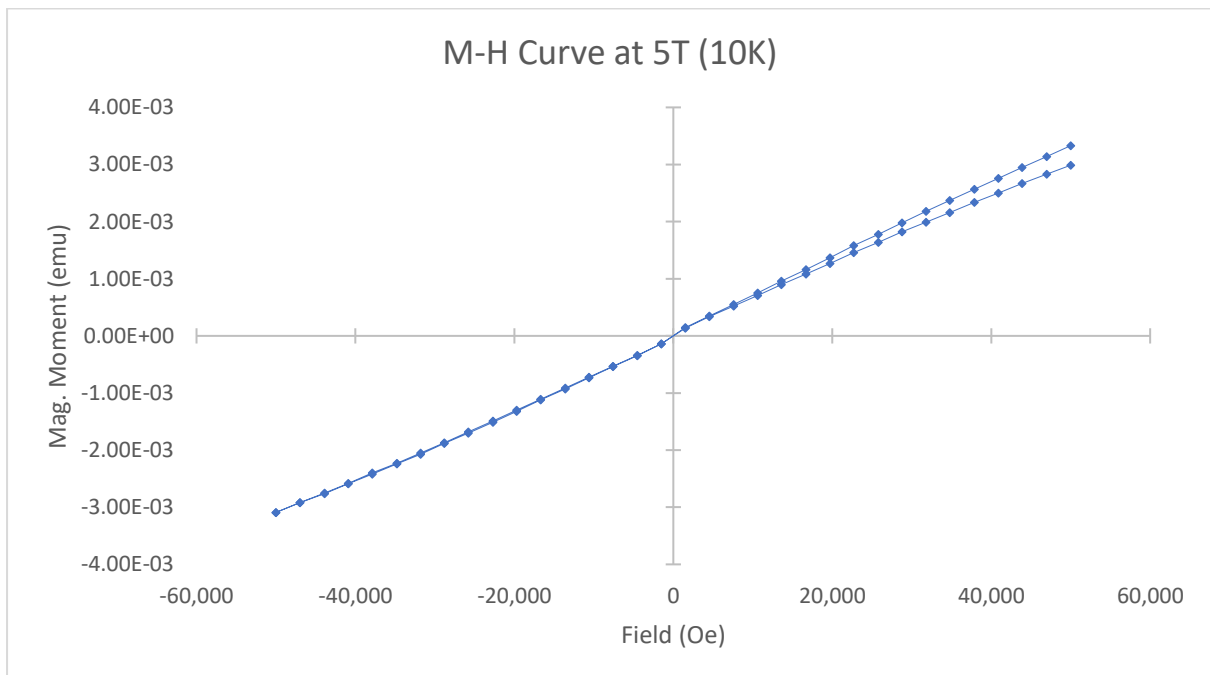


**Figure 12:** MH curve at 5T, 10K

The measurement was carried out below the ordering temperature, which explains the approximately linear relation between the two parameters. As the measurement was initiated at a +5T magnetic field and was decreased to -5T and then increased back to +5T, the lines formed from the joined data points do not perfectly match each other. This can be seen at -2T and more clearly above +2T. The reason for this may be due to a remnant magnetisation of the material.

#### 4.5 SEM-EDS

The scanning electron microscope was used to take images of single crystals of both compounds. For  $\text{CaBaCo}_2\text{Fe}_2\text{O}_7$ , a small amount sample 7 was used. The sample was coated with a 10 nm layer of gold. The image (Figure 13) was taken using a spot size of 5.0 and a voltage of 5 kV.

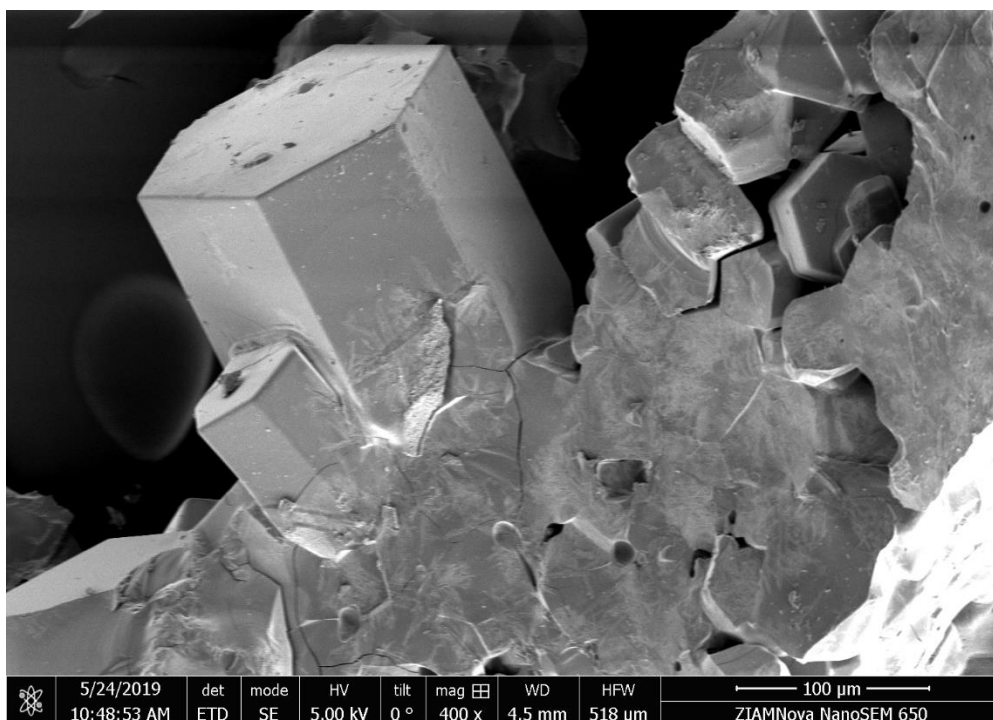


*Figure 13: SEM image of a single crystal of  $\text{CaBaCo}_2\text{Fe}_2\text{O}_7$  (Sample 7)*

The largest crystal in figure 8 has a dimension of approximately  $150\ \mu\text{m}$  in its a-b plane. This crystal was one of the largest in the sample and the average crystal size for the whole sample was approximately  $100\ \mu\text{m}$ . The single crystals that formed usually formed were short and wide, or long and thin crystals.

The EDS analysis was used to measure the ratio of each element per formula unit for the sample. A spot size of 5.0 and a voltage of 18 kV was used for this measurement. The amounts of each element present are shown in Table 7.

Element	Atomic percentage
Ca	8%
Ba	8%
Fe	13%
Co	16%

*Table 7: EDS results for  $\text{CaBaCo}_2\text{Fe}_2\text{O}_7$  (Sample 7)*

The rest of the elements present are carbon, gold, oxygen and other impurities such as aluminium. The ratio of both Ca to Ba and Fe to Co are mostly one to one, and the ratios between Fe and Co to Ca and Ba are mostly two to one. The small discrepancies in the percentage are mostly due to experimental error in weighing out the initial precursors, or they could also be due to the presence of the starting materials. The graph used to calculate this data is shown in Figure 14.

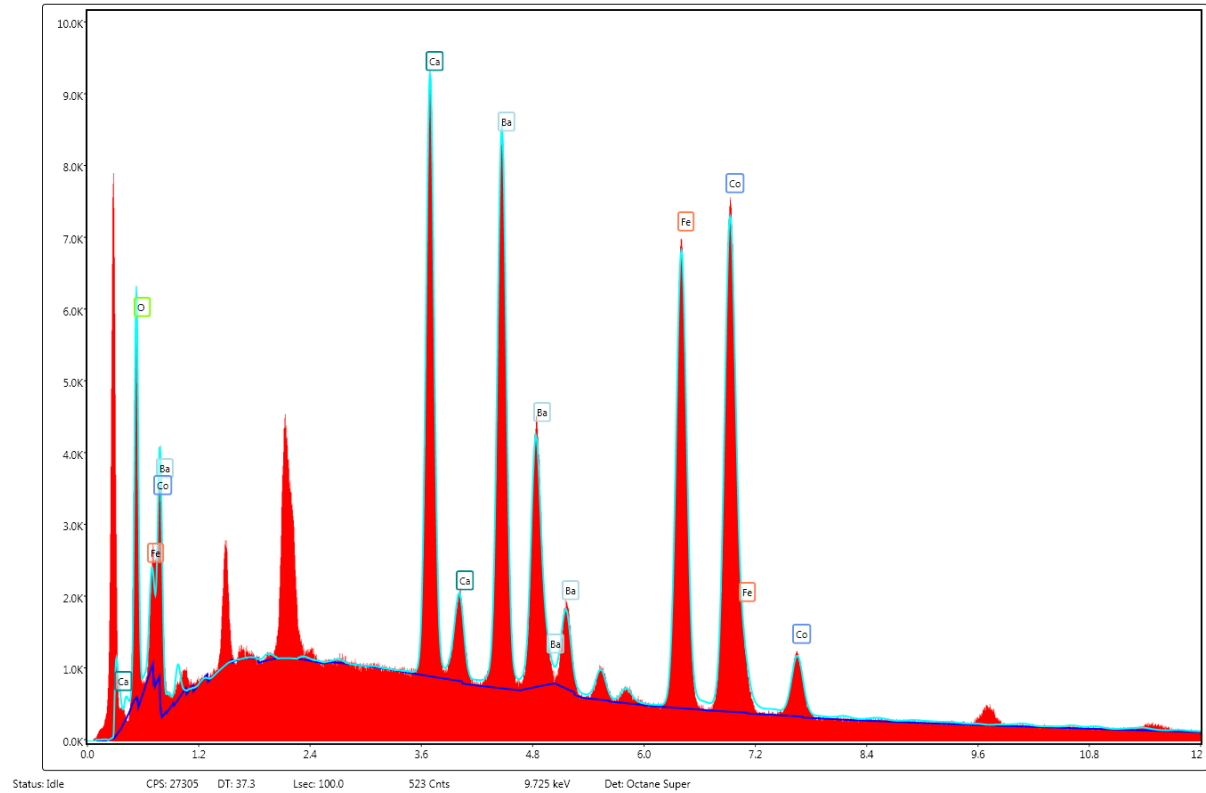


Figure 14: EDS graph of  $\text{CaBaCo}_2\text{Fe}_2\text{O}_7$

The elements corresponding to each peak are shown on the graph. The unmarked peaks all correspond to either aluminium (from the crucible) or gold (due to the coating for the SEM).

The electron microscope was used to view the crystals from samples 17a-c, and an EDS measurement was taken on both crystal types found in the mixed-flux crystal mixture. The results are displayed in Tables 8&9.

Element	Atomic Percentage
Ca	1%
Ba	< 1%
V	< 1%
Co	82%
O	17%

Element	Atomic Percentage
Ca	38%
Ba	< 1%
V	18%
Co	< 1%
O	26%
Cl	18%

Tables 8 (left) & 9 (right): Atomic composition of dark octahedral crystals (Sample 17c, left) & of blocky transparent crystals (Sample 17c, right)

The large fraction of Cobalt in the octahedral crystals along with a smaller fraction of oxygen can prove that the octahedral single crystals that were made are in fact, cobalt (II,II) oxide. According to the EDS measurement, only trace amounts of calcium, barium and vanadium are present in the crystals, but what is alarming is that both substances from the sample only have trace amounts of barium. This is quite strange, as the absence of one element in one substance can be explained by a

dominant presence in the other substance in the same reaction mixture, for example: the octahedral crystals contain 82% cobalt and the transparent crystals contain less than 1%. The reason for this absence is due to the possibility that the barium in the reaction mixture somehow got absorbed by the barium chloride flux, which was then removed after the crystal growth process. It is also possible that the spots chosen to measure their composition just had a larger deficit of a certain element than others. To fix this issue, the measurement should be carried out on more spots of the same sample. The crystals of both compounds can be found in the images below. The octahedral crystals of  $\text{Co}_3\text{O}_4$  and  $\text{Ca}_2(\text{VO}_4)\text{Cl}$  are shown in Figures 15&16. The rest of the SEM images can be found in Appendix D: Figures 31-34.

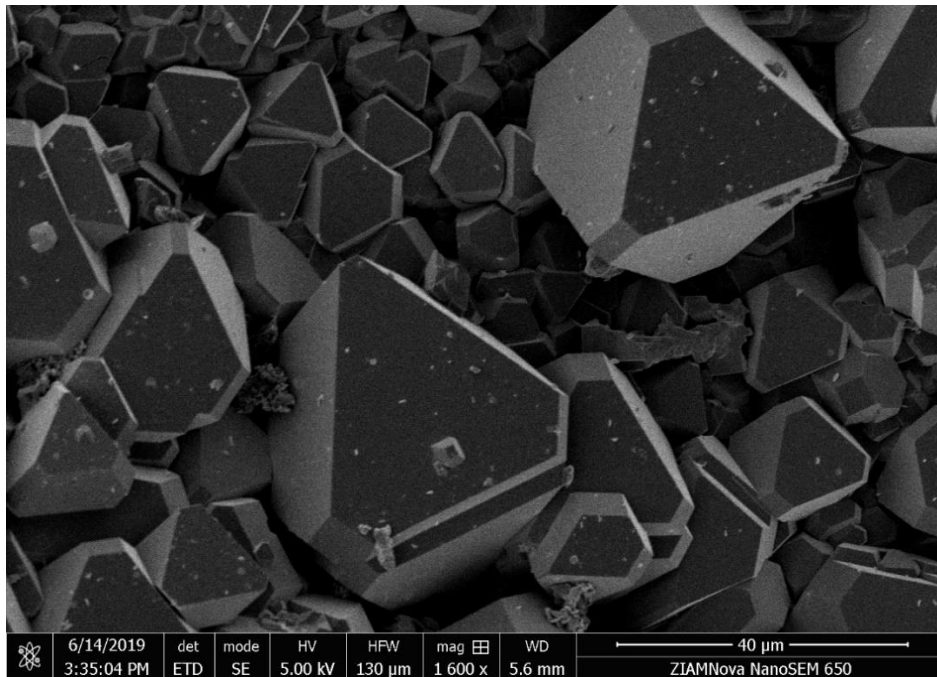


*Figure 15: Truncated octahedral crystals of  $\text{Co}_3\text{O}_4$  (Sample 17c)*

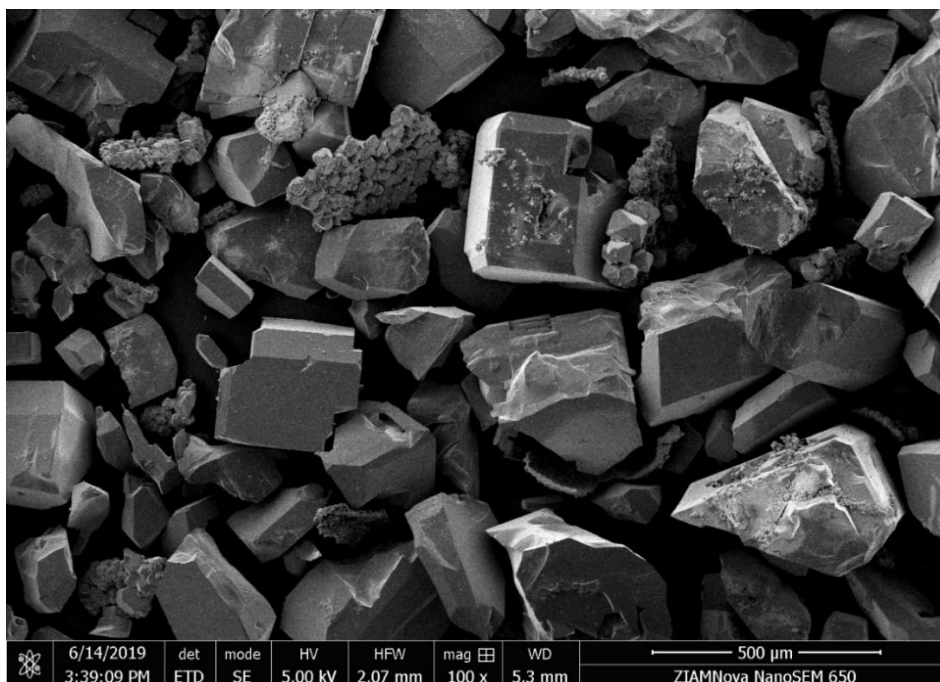


*Figure 16: Transparent, blocky crystals of  $\text{Ca}_2(\text{VO}_4)\text{Cl}$  (Sample 17c)*

## 5. CONCLUSIONS

This research project involved the attempted synthesis and characterisation of two Swedenborgite compounds,  $\text{CaBaCo}_2\text{Fe}_2\text{O}_7$  and  $\text{CaBaCo}_2\text{V}_2\text{O}_7$ . The two compounds were synthesized using a solid-state reaction between individual metal oxides and metal carbonates. For the iron-containing material, synthesis at  $1000^\circ\text{C}$  with a two-day heating in a platinum crucible yielded the best result, due to its inert properties. This lower temperature gave better results than synthesis at  $1100^\circ\text{C}$ , as less cobalt oxide vaporised. EDS measurements were used to determine the atomic ratios of each element in the compound. The results were very close to the molecular formula, however small deviations were found. The element with the largest deviation was found to be cobalt, however this was most likely due to the side reaction and the vaporisation of cobalt oxide during synthesis. Regardless of the lack of purity in all synthesised samples, the solid-state reaction method proved suitable for all of the analysis techniques employed in this project.

When viewing the single crystals grown using the flux growth under the SEM, it was found that the crystals were not hexagonal, but truncated octahedra. This, along with the EDS results, and the magnetization data, it was confirmed that cobalt(II,III) oxide single crystals were formed in the flux growth. The almost-complete absence of barium was most likely due to the flux absorbing it out of the reaction mixture.

Hexagonal crystals were grown by cooling the iron-containing sample from  $1200^\circ\text{C}$  to room temperature for 21 hours. The vanadium-based compound had to be synthesised under an argon/hydrogen atmosphere to prevent the oxidation of vanadium at high temperatures. Similar crystals were also grown using a 37%:63% ratio of  $\text{BaCl}_2$  to  $\text{CaCl}_2$  in a nitrogen atmosphere, by heating to  $950^\circ\text{C}$  and cooling for approx. 96 hours. This mixed flux resulted in the best crystal growth, most likely due to its lowest melting temperature, however much smaller crystals were also grown using the two separate fluxes. One method for growing crystals that may be useful is the float zone crystal growth, however since a pure powder sample must first be prepared for this method, a different synthetic strategy should be examined.

All synthesised compounds were analysed using powder x-ray diffraction. All syntheses in the alumina crucibles resulted in the formation of cobalt aluminate, which was found in the XRD spectra, but also on the walls of the crucible that was used. One impurity that was found in every PXRD spectrum was  $\text{Co}_3\text{O}_4$ . From this we can conclude that the cobalt oxide that didn't react with the alumina crucible settled back into the reaction mixture as it was cooling. All attempts of limiting cobalt oxide as an impurity during synthesis were unsuccessful, including a lower reaction temperature, and a longer reaction time. The analysis of what was thought to be  $\text{CaBaV}_2\text{Co}_2\text{O}_7$  resulted in the  $P3_1c$  space group. Again, the samples were impure due to the vaporization of cobalt oxide and the presence of aluminates.

The single crystal diffraction data of  $\text{CaBaCo}_2\text{Fe}_2\text{O}_7$  resulted in the  $P6_3mc$  space group with hexagonal symmetry. This was confirmed with powder XRD. The crystal structure was solved using Bruker APEX3 software and it was found that the compound consists of an ABAB-layered system containing cobalt oxide and barium oxide tetrahedra on one layer, along with iron oxide tetrahedra and calcium oxide octahedra in the other layer. It was found that the crystal structure was identical to what was reported by Valldor. The precession images show reflections which all obey the reflection conditions for the  $P6_3mc$  space group. The lattice parameters of the crystal were found to be  $a = 6.331 \text{ \AA}$ ,  $b = 6.331 \text{ \AA}$  and  $c = 10.2322 \text{ \AA}$ , with angles  $\alpha = 90^\circ$ ,  $\beta = 90^\circ$  and  $\gamma = 120^\circ$ . This, along with the calculated space group proves the hexagonal geometry of the compound. The single crystals grown from the solid-state reaction of the vanadium-based compound were found to be barium vanadate –  $\text{Ba}_3(\text{VO}_4)_2$ , which

belongs to the  $R\bar{3}$  space group with rhombohedral geometry. The dark crystals that were formed during the synthesis were not analysed, due to their amorphous nature. The crystals that were made using flux growth were confirmed to be cobalt (II,III) oxide with cubic geometry and calcium vanadate chloride –  $\text{Ca}_2(\text{VO}_4)\text{Cl}$  with orthorhombic geometry. From these two vanadate compounds we can conclude that the vanadium has oxidized in both cases to vanadium(V). In  $\text{CaBaV}_2\text{Co}_2\text{O}_7$  it needs to remain in the +3 oxidation state. The compound created using the calcium chloride flux was not identified, however its point group was found to be  $P2_1c$  with monoclinic geometry. Along with the reasoning that the flux reacted with the product, we can conclude that both flux growth and traditional crystallization were both unsuitable for the target compound.

The magnetic susceptibility versus temperature showed two peaks in the zero-field cooling measurement, at 140K and 50K. Above 200K the field-cooled and zero-field cooled measurements were almost identical, with a transition to paramagnetic behaviour above 750K. The resulting data does not obey the Curie-Weiss law above 200 K which would rule out antiferromagnetic behaviour. However, this contradicts the two peaks found below this temperature, which serve as evidence for the presence of an antiferromagnet. The M-H curves at 10K and 100K also show hysteresis. From the magnetic measurements, we can conclude that the iron-containing swedenborgite shows both antiferromagnetic and ferromagnetic behaviour at low temperatures, however it has not been confirmed yet if either of these behaviours is due to the presence of an impurity. The reason for this is that the induced magnetic moment is too high to be coming from an impurity, and it is too low to be purely from the magnetic material. The magnetic properties of the flux-grown crystals show antiferromagnetic behaviour, with an ordering temperature of 35K, which is in agreement with what was reported in literature.

## 6. OUTLOOK

There are a few aspects in this research project that can be improved and investigated more. The most important part that should be improved is the synthetic method of both compounds. All of the samples that were made over the course of this project were impure. One suggestion would be to look into a synthesis that doesn't allow the cobalt oxide to vaporize, and then settle back into the reaction mixture upon cooling. Once a new method is found that results in pure samples, the floating zone method can be used to grow large single crystals. Similarly, for  $\text{CaBaV}_2\text{Co}_2\text{O}_7$ , a method that keeps the vanadium in the correct oxidation state should be employed, along with a method to grow crystals that doesn't interfere with the target compound. Different synthetic methods (e.g. Sol-gel synthesis) should be tested to see if the properties of the target compound are affected. The magnetic properties measurements for a single crystal were unsuccessful in this project, so another target of investigation would be to get measurements in both the a-b and c planes of the hexagonal  $\text{CaBaFe}_2\text{Co}_2\text{O}_7$  crystals, to see if the induced magnetic moment would be higher than what was measured, and what dependence the magnetic moment has on crystal orientation, if any. The crystal structure of the material from the calcium chloride flux should also be identified. As for investigating different materials, different ratios of cobalt to iron/vanadium should be tested, and also different elements with similar properties to the three metals could be investigated.

## 7. APPENDICES

### 7.1. Appendix A

SAMPLE NO.	TARGET COMPOUND	SYNTHESIS CONDITIONS	HEATING TIME	CRUCIBLE TYPE	Comments
1	CaBaCo <sub>2</sub> Fe <sub>2</sub> O <sub>7</sub>	1100°C	1 day	Alumina	
2	CaBaCo <sub>2</sub> Fe <sub>2</sub> O <sub>7</sub>	1100°C	2 days	Alumina	Continued from Sample 1
3	CaBaCo <sub>2</sub> Fe <sub>2</sub> O <sub>7</sub>	1000°C	1 day	Alumina	
4	CaBaCo <sub>2</sub> Fe <sub>2</sub> O <sub>7</sub>	1200°C	4 hours (cooling)	Alumina	Hexagonal Single Crystals from Sample 2 (CaBaFe <sub>2</sub> Co <sub>2</sub> O <sub>7</sub> )
5	CaBaCo <sub>2</sub> Fe <sub>2</sub> O <sub>7</sub>	1100°C	1 day	Platinum	
6	CaBaCo <sub>2</sub> Fe <sub>2</sub> O <sub>7</sub>	1200°C	4 hours (cooling)	Alumina	Polycrystals from Sample 2 (CaBaFe <sub>2</sub> Co <sub>2</sub> O <sub>7</sub> )
7	CaBaCo <sub>2</sub> Fe <sub>2</sub> O <sub>7</sub>	1200°C	21 hours (cooling)	Alumina	Hexagonal Single Crystals from Sample 3 (CaBaFe <sub>2</sub> Co <sub>2</sub> O <sub>7</sub> )
8	CaBaCo <sub>2</sub> Fe <sub>2</sub> O <sub>7</sub>	1100°C	1 day	Platinum	
9	CaBaCo <sub>2</sub> Fe <sub>2</sub> O <sub>7</sub>	1000°C	1 day	Alumina	PXRD sample (from Sample 8)
10	CaBaCo <sub>2</sub> Fe <sub>2</sub> O <sub>7</sub>	1000°C	1 day	Alumina	
11	CaBaCo <sub>2</sub> V <sub>2</sub> O <sub>7</sub>	1000°C	1 day	Alumina	
12	CaBaCo <sub>2</sub> V <sub>2</sub> O <sub>7</sub>	1000°C	2 days	Alumina	Continued from Sample 11 (H <sub>2</sub> /Ar atm.)
13	CaBaCo <sub>2</sub> V <sub>2</sub> O <sub>7</sub>	1100°C	24 hours (cooling)	Alumina	Layered Transparent Crystals Ba <sub>3</sub> (VO <sub>4</sub> ) <sub>2</sub>
14	CaBaCo <sub>2</sub> V <sub>2</sub> O <sub>7</sub>	1100°C	24 hours (cooling)	Alumina	Amorphous Purple Crystals (unidentified)
15	CaBaCo <sub>2</sub> V <sub>2</sub> O <sub>7</sub>	1100°C	24 hours (cooling)	Alumina	Single Crystals (unidentified)
16	CaBaCo <sub>2</sub> V <sub>2</sub> O <sub>7</sub>	1000°C	24 hours	Alumina (Tube Furnace)	Nitrogen Atmosphere
17a	CaBaCo <sub>2</sub> V <sub>2</sub> O <sub>7</sub>	1050°C	96 hours (cooling)	Alumina (Tube Furnace)	BaCl <sub>2</sub> flux growth (Ca <sub>2</sub> (VO <sub>4</sub> )Cl + Co <sub>3</sub> O <sub>4</sub> )
17b	CaBaCo <sub>2</sub> V <sub>2</sub> O <sub>7</sub>	1000°C	96 hours (cooling)	Alumina (Tube Furnace)	CaCl <sub>2</sub> flux growth (unidentified)
17c	CaBaCo <sub>2</sub> V <sub>2</sub> O <sub>7</sub>	950°C	96 hours (cooling)	Alumina (Tube Furnace)	BaCl <sub>2</sub> + CaCl <sub>2</sub> flux growth (Ca <sub>2</sub> (VO <sub>4</sub> )Cl + Co <sub>3</sub> O <sub>4</sub> )

**Table 10:** List of all tested samples

## 7.2. Appendix B

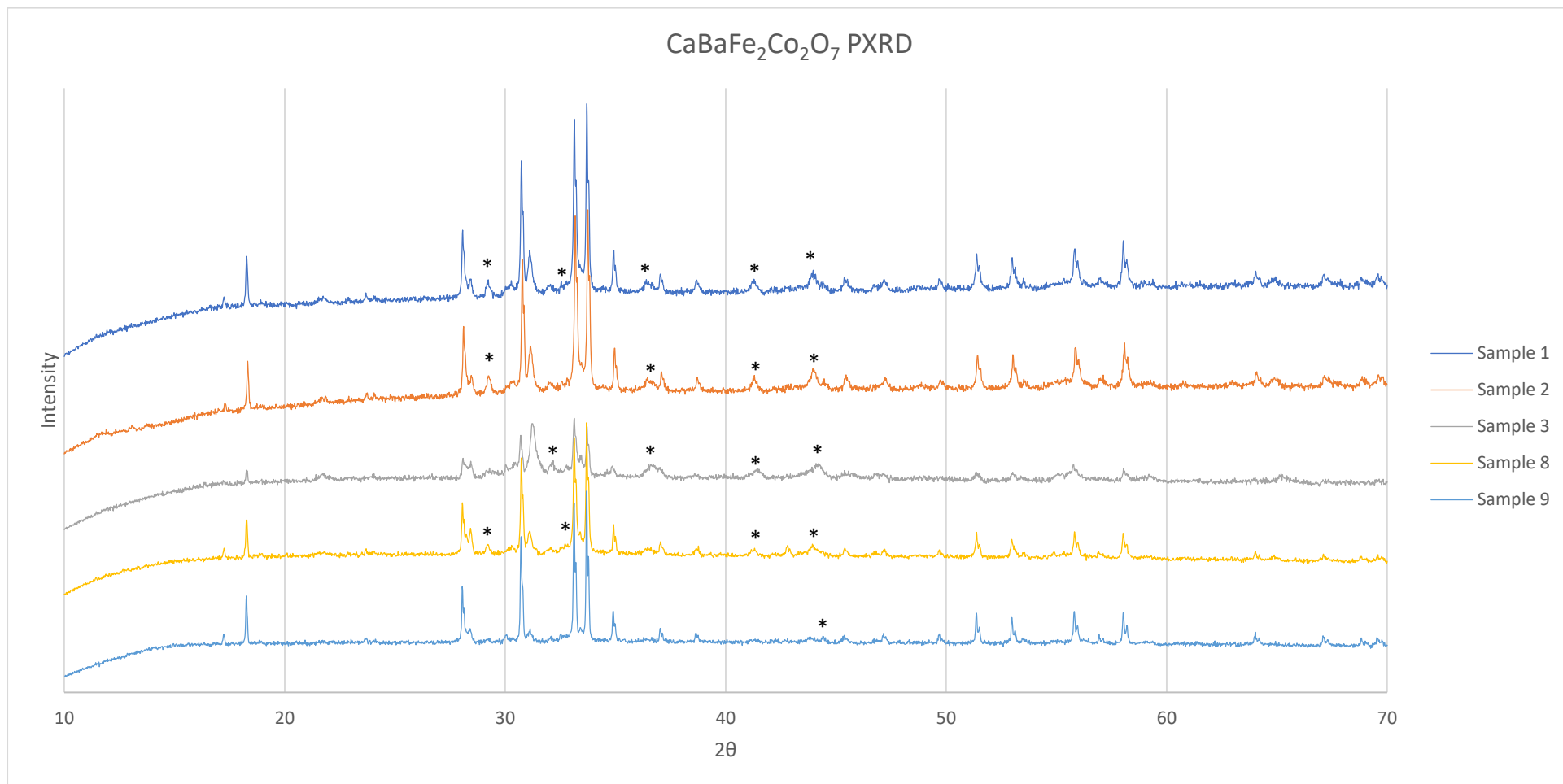


**Figure 17:** PXRD results of  $\text{CaBaCo}_2\text{Fe}_2\text{O}_7$  (impurities marked with a star)

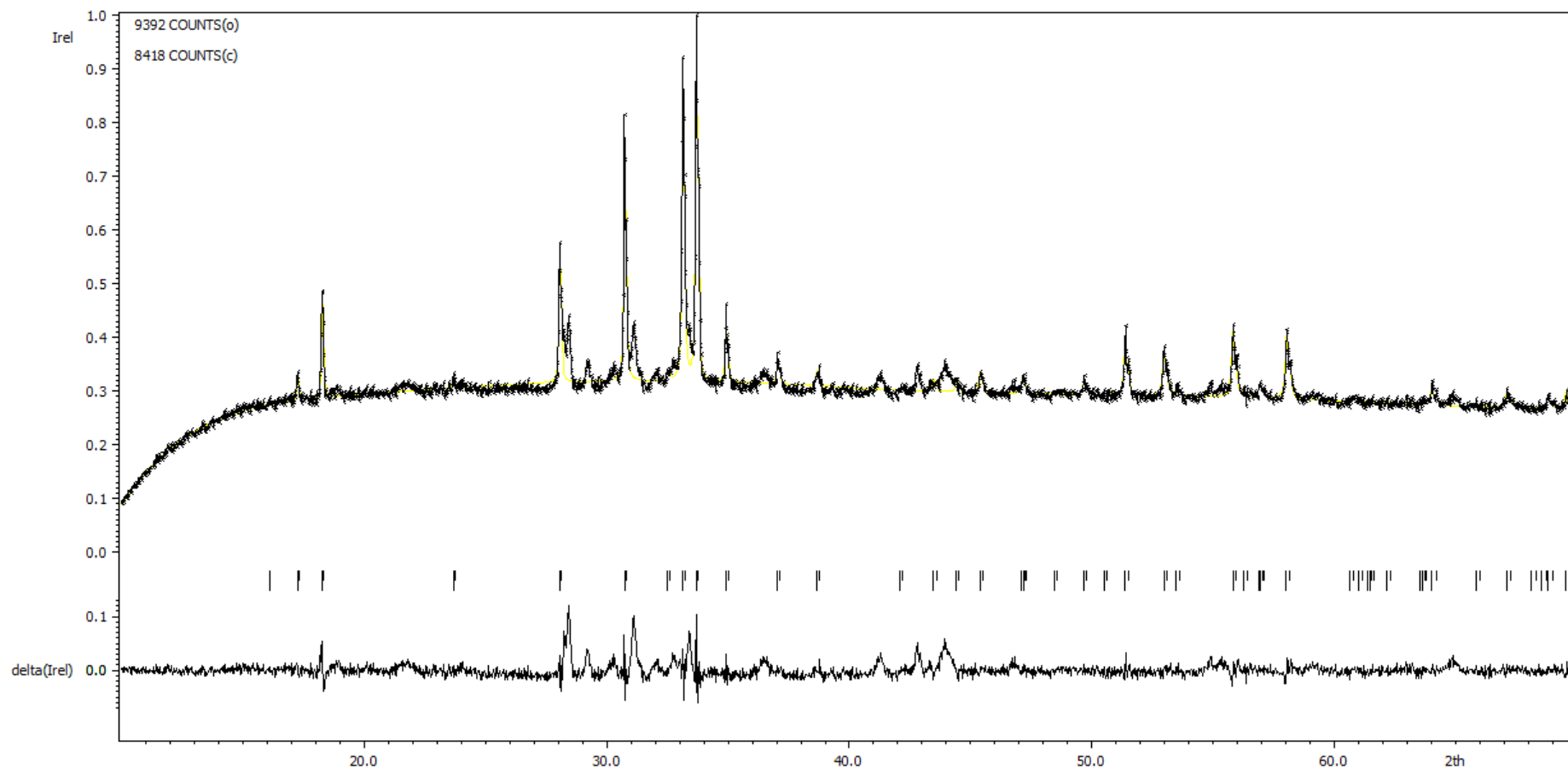
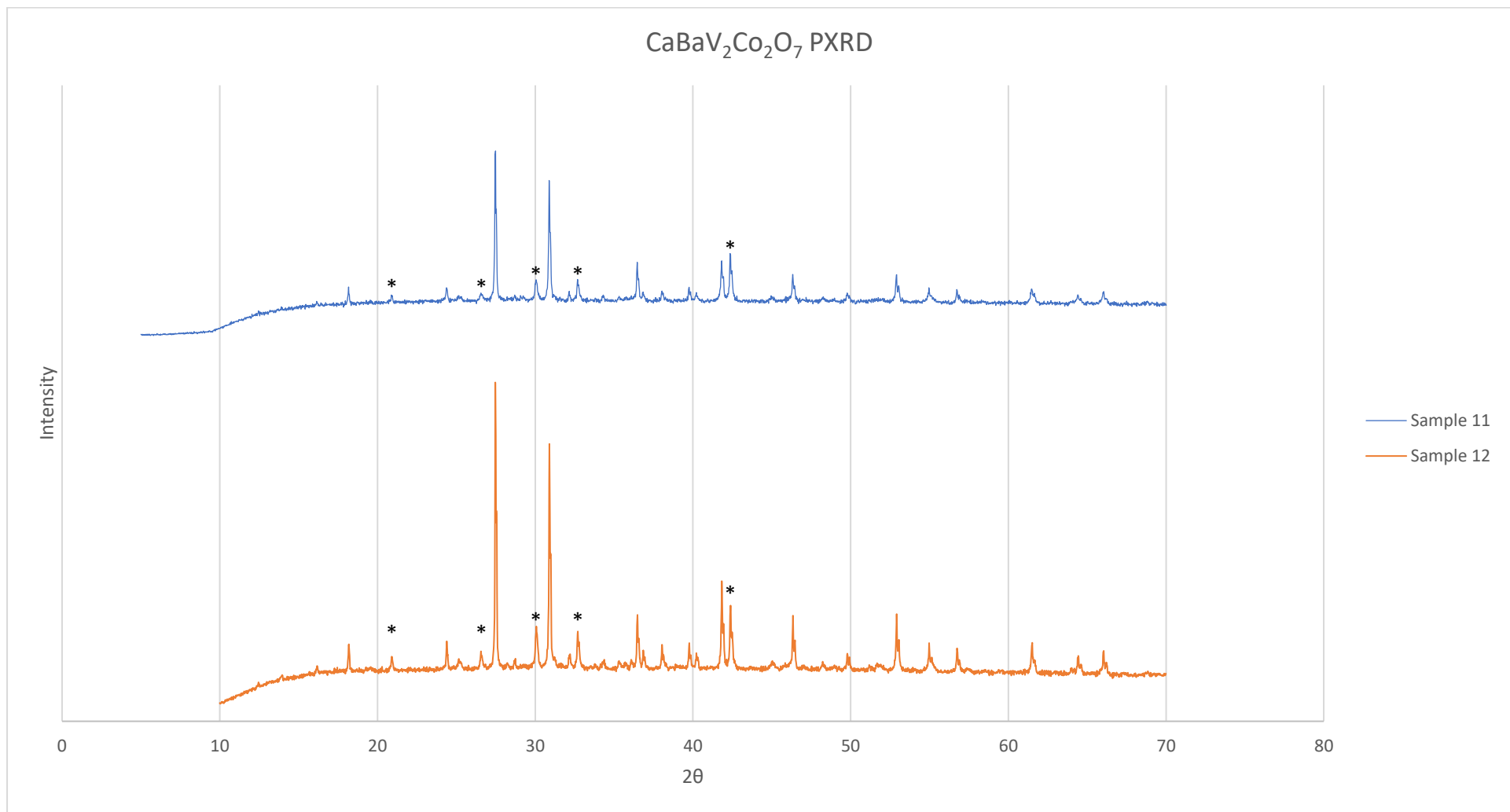


Figure 18: PXRD data of Sample 8 (With calculated fits)



**Figure 19:** PXRD results of CaBaV<sub>2</sub>Co<sub>2</sub>O<sub>7</sub> (impurities marked with a star)

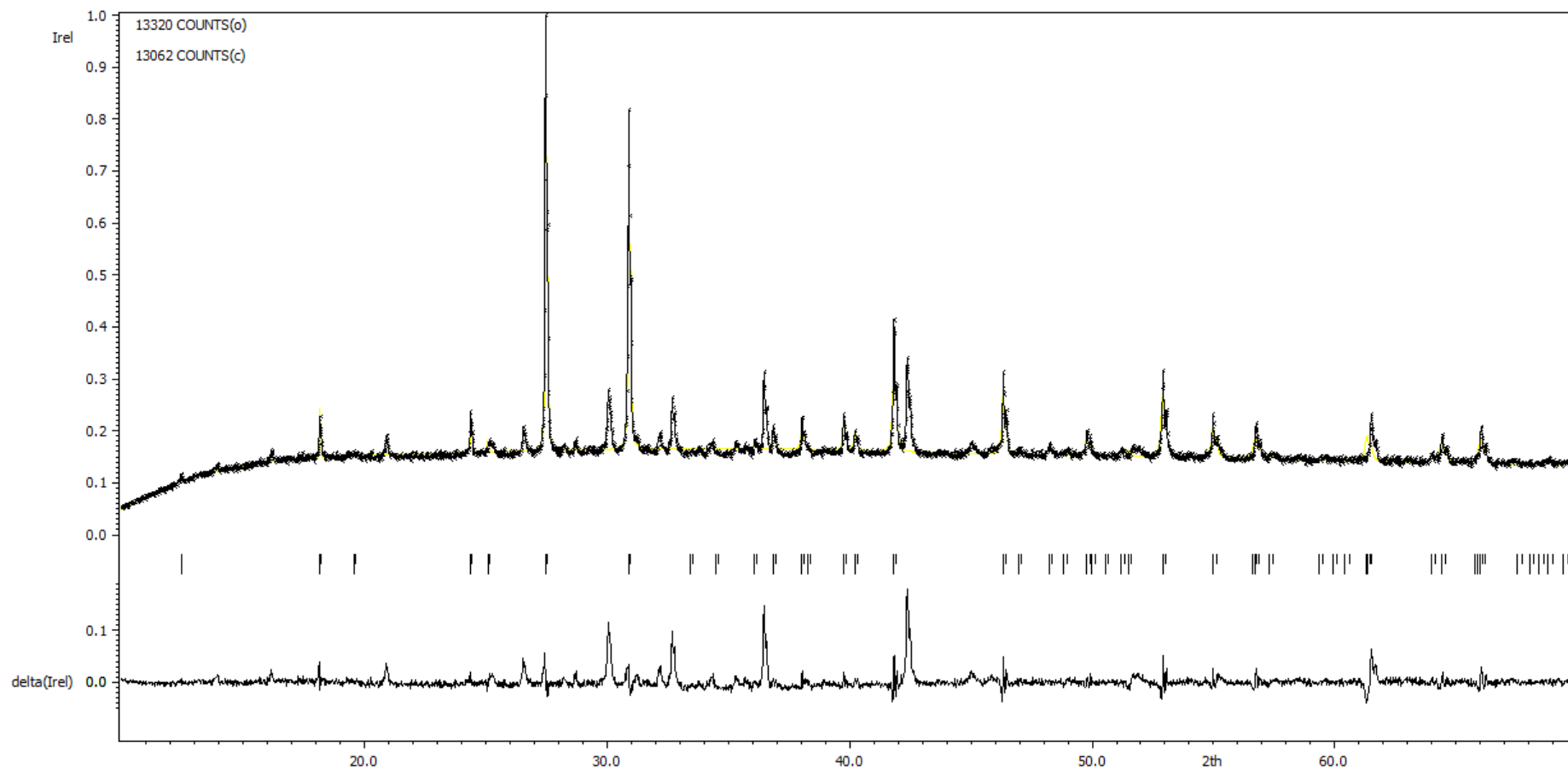
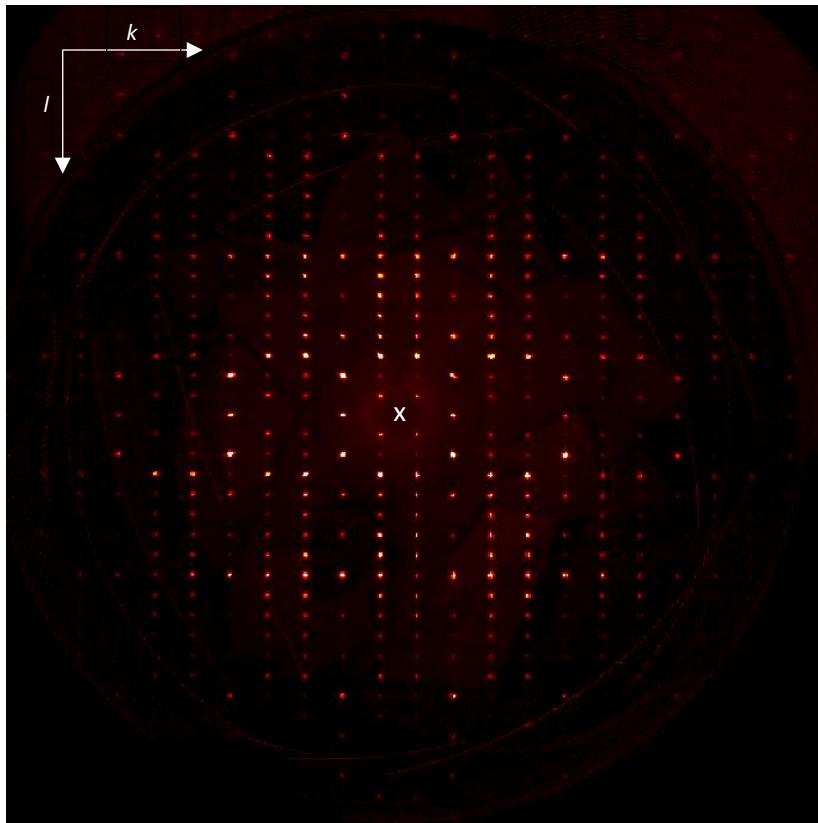
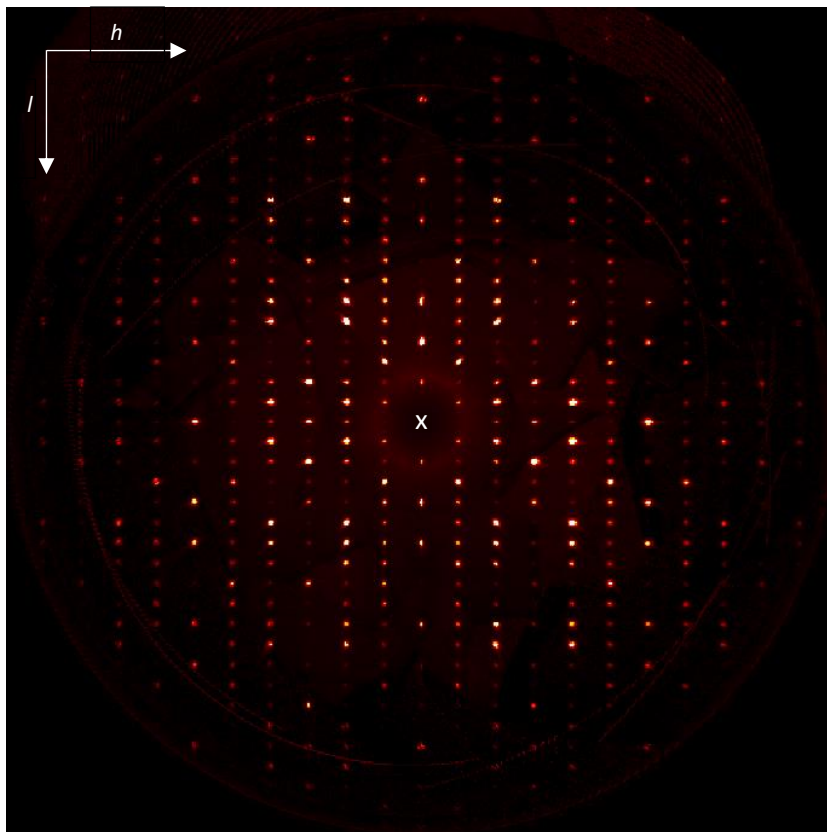


Figure 20: PXRD data of Sample 12 (With calculated fits)

### 7.3. Appendix C



**Figure 21:** Precession images of  $1kl$  reciprocal planes of  $\text{CaBaCo}_2\text{Fe}_2\text{O}_7$  ( $k=0, l=0$  marked by white "x")



**Figure 22:** Precession images of  $h0l$  reciprocal planes of  $\text{CaBaCo}_2\text{Fe}_2\text{O}_7$  ( $h=0, l=0$  marked by white "x")

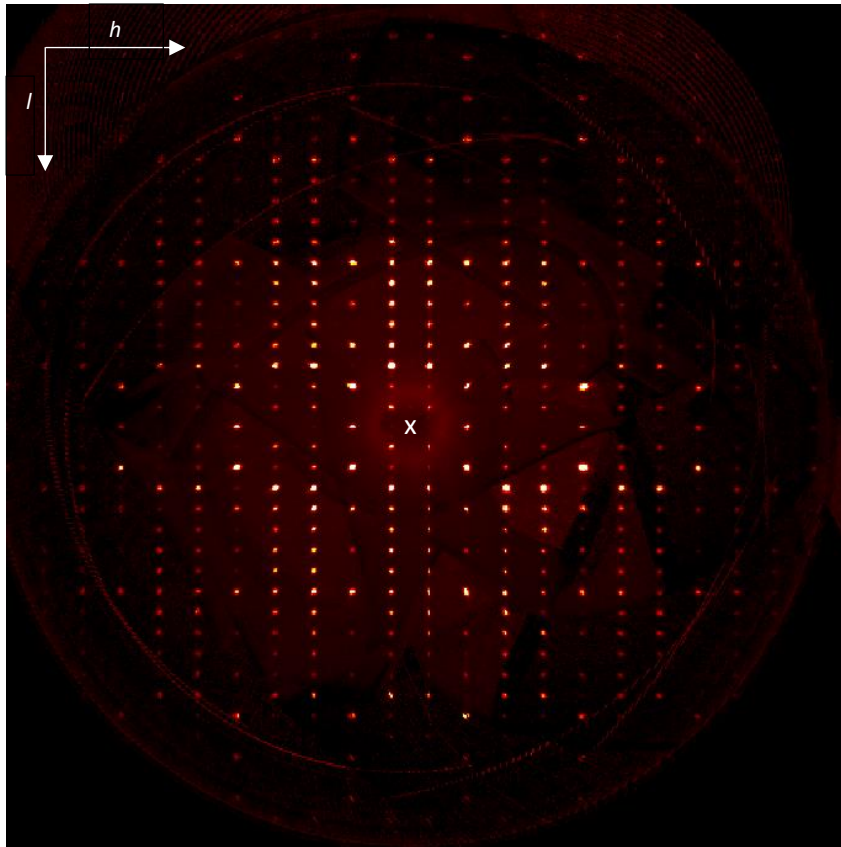


**Figure 23:** Precession images of  $h1l$  reciprocal planes of  $\text{CaBaCo}_2\text{Fe}_2\text{O}_7$  ( $h=0, l=0$  marked by white "x")

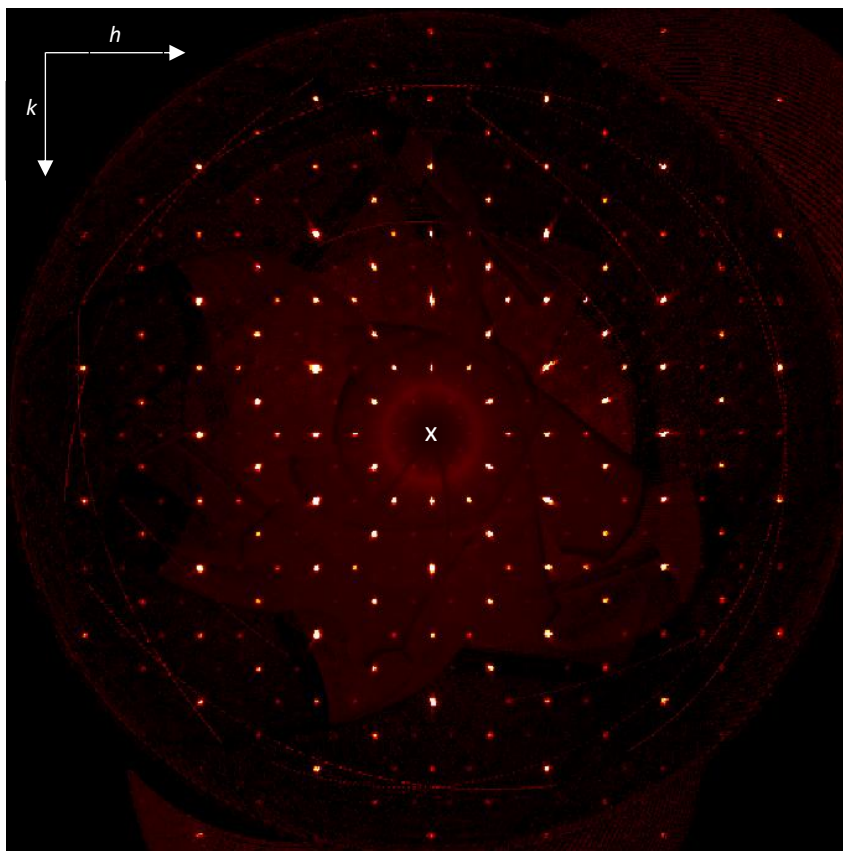


**Figure 24:** Precession images of  $hk0$  reciprocal planes of  $\text{CaBaCo}_2\text{Fe}_2\text{O}_7$  ( $h=0, k=0$  marked by white "x")

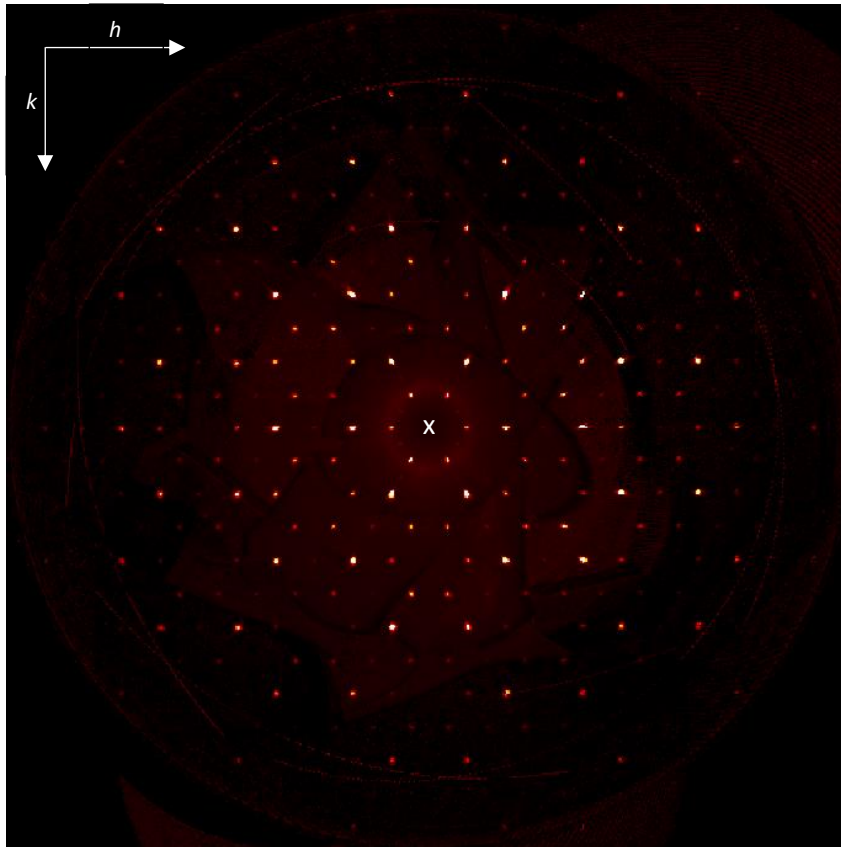


**Figure 25:** Precession images of  $hk1$  reciprocal planes of  $\text{CaBaCo}_2\text{Fe}_2\text{O}_7$  ( $h=0$ ,  $k=0$  marked by white "x")

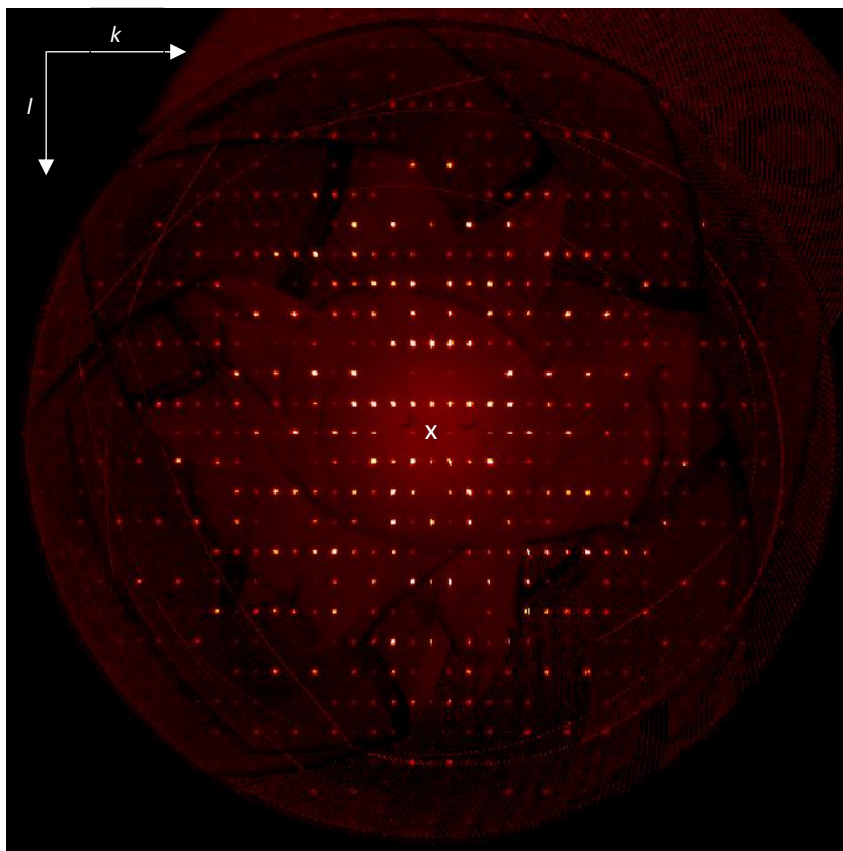


**Figure 26:** Precession image of  $1kl$  reciprocal plane of the unidentified compound in Sample 17b ( $k=0$ ,  $l=0$  marked by white "x")

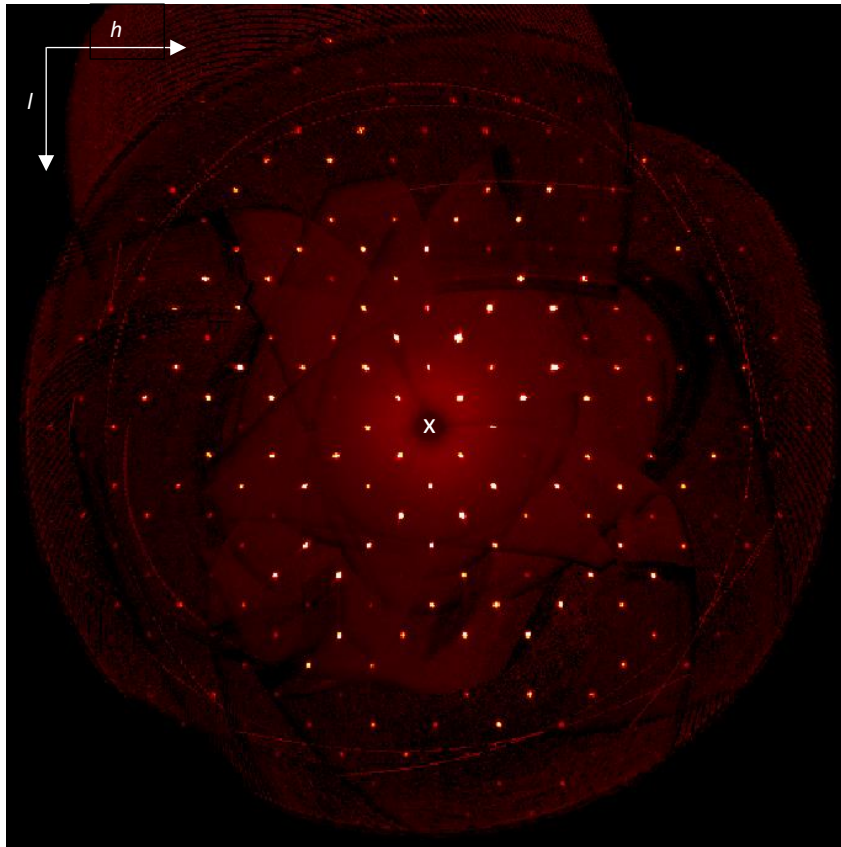


**Figure 27:** Precession image of  $h0l$  reciprocal plane of the unidentified compound in Sample 17b ( $h=0, l=0$  marked by white "x")

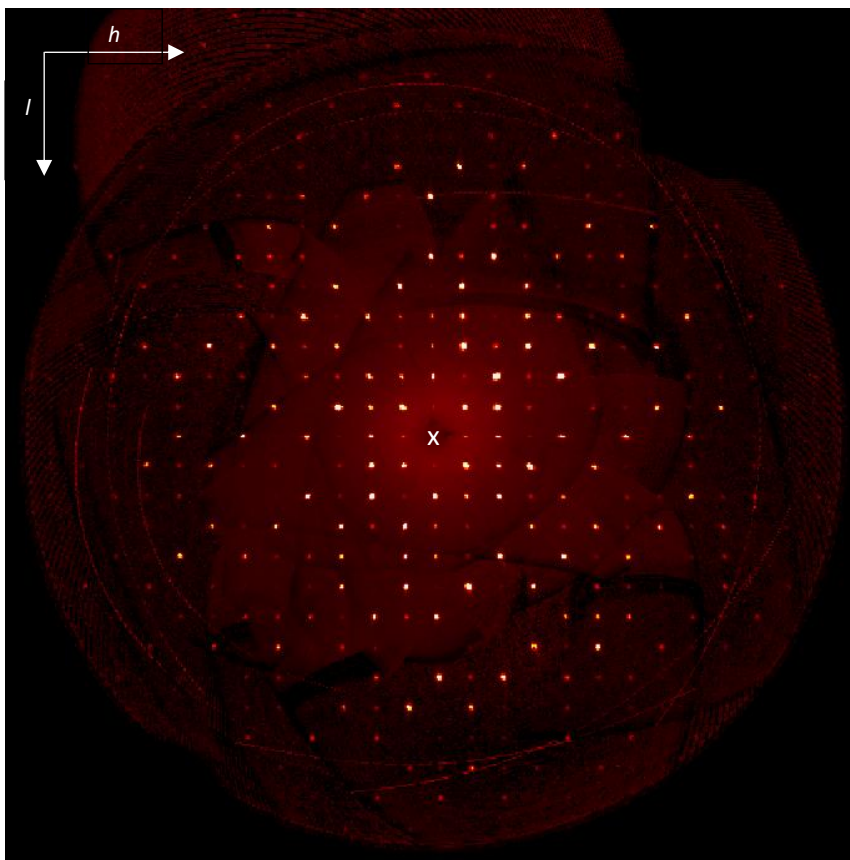


**Figure 28:** Precession image of  $h1l$  reciprocal plane of the unidentified compound in Sample 17b ( $h=0, l=0$  marked by white "x")

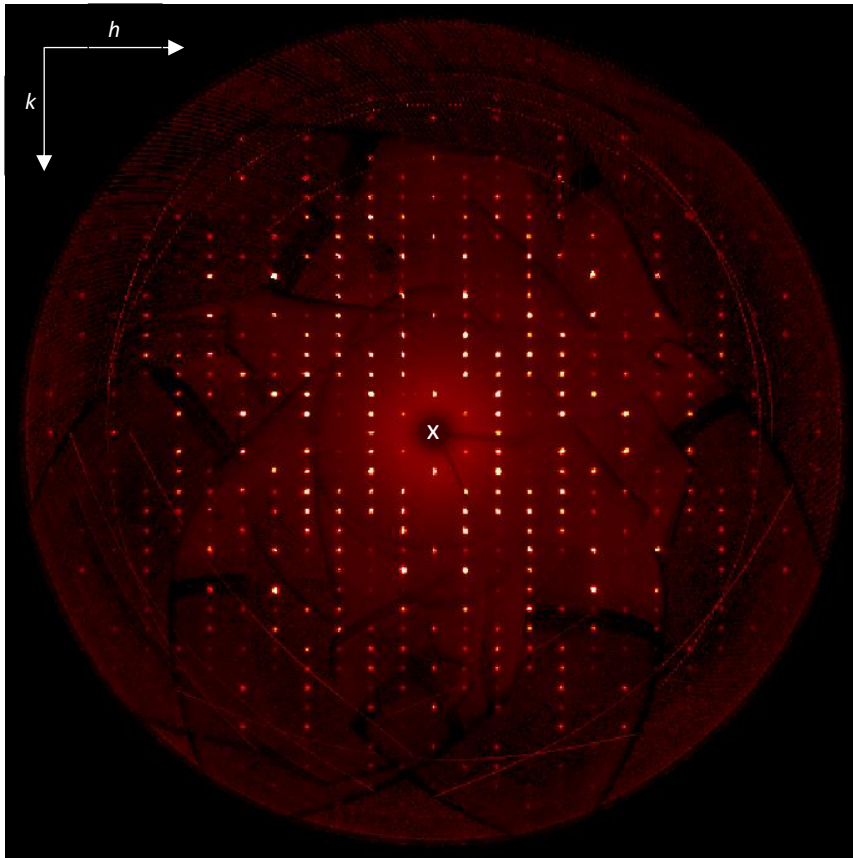


**Figure 29:** Precession image of  $hk0$  reciprocal plane of the unidentified compound in Sample 17b ( $h=0, k=0$  marked by white "x")

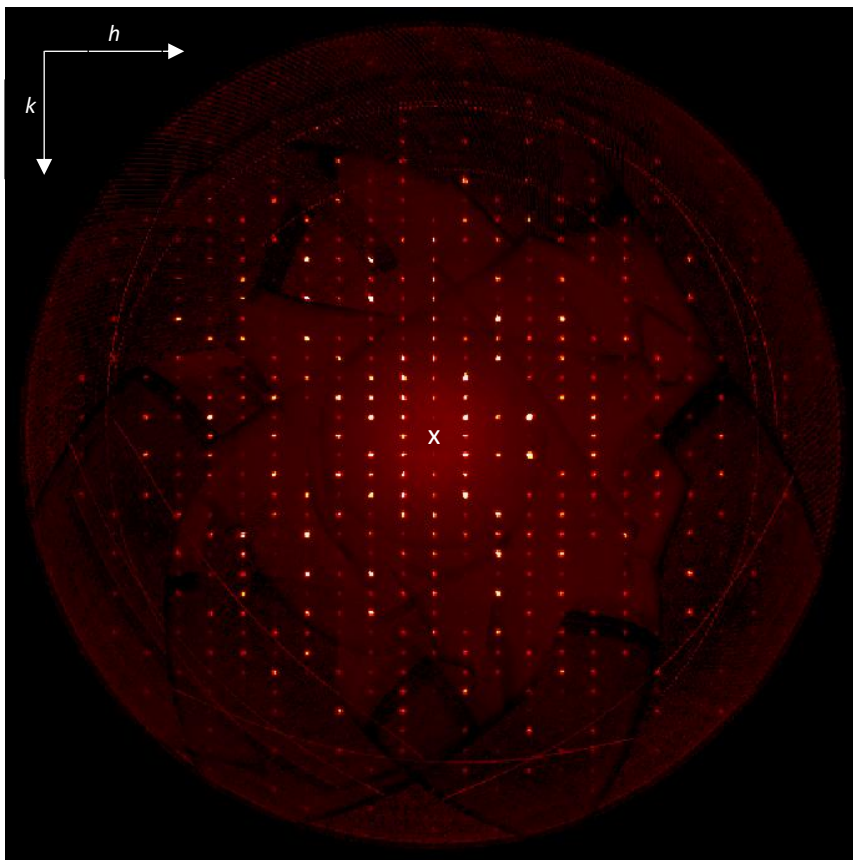


**Figure 30:** Precession image of  $hk1$  Reciprocal plane of the unidentified compound in Sample 17b ( $h=0, k=0$  marked by white "x")

## 7.4 Appendix D

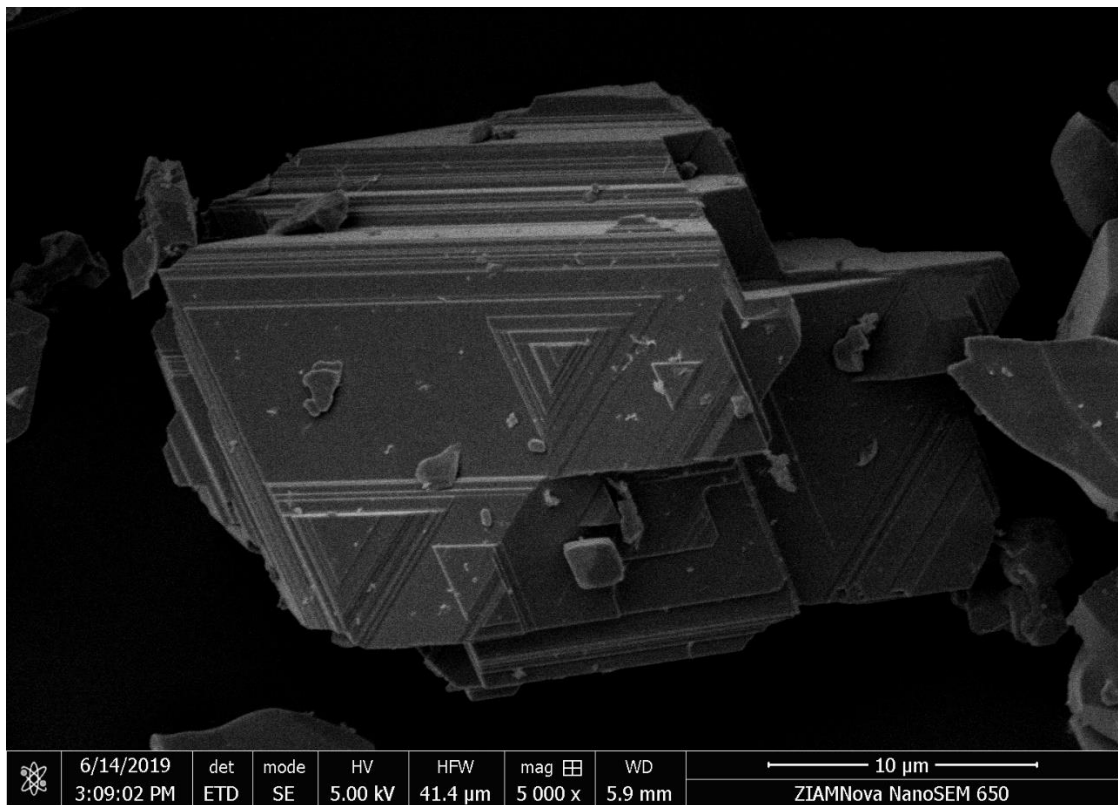


Figure 31: SEM image of a crystal grown using  $\text{BaCl}_2$  flux. (Sample 17a)

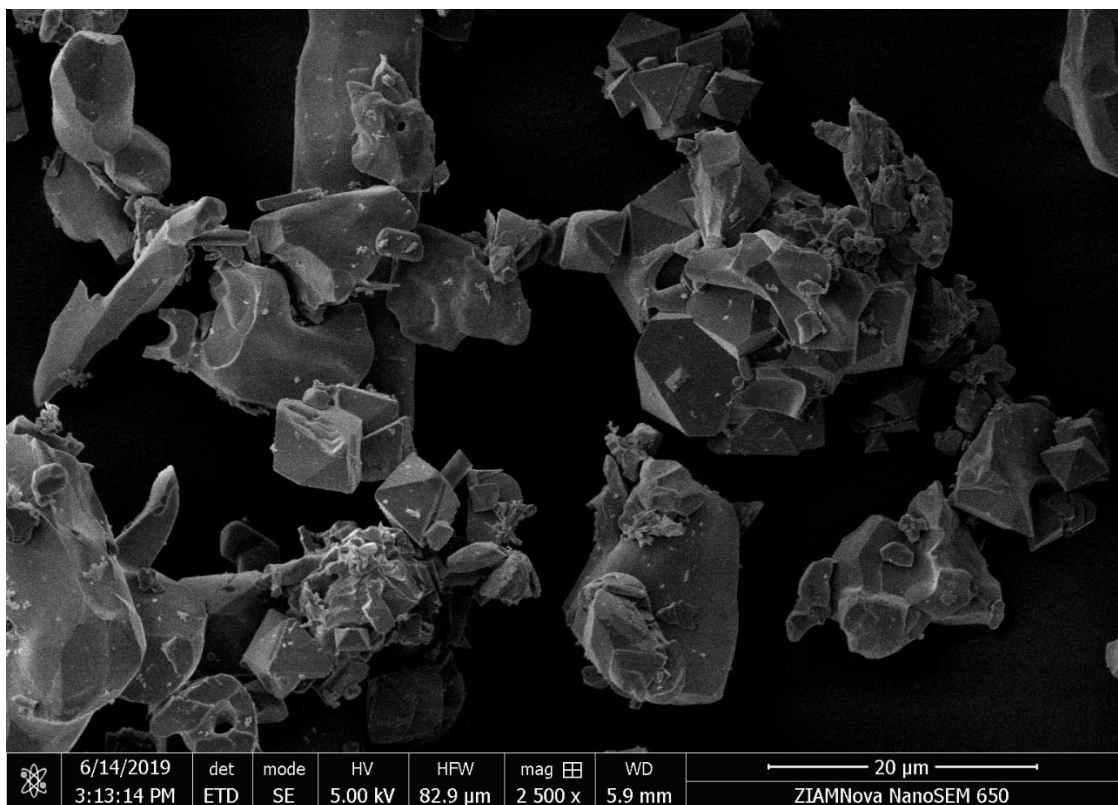


Figure 32: SEM image of octahedral crystals grown using  $\text{BaCl}_2$  flux. (Sample 17a)

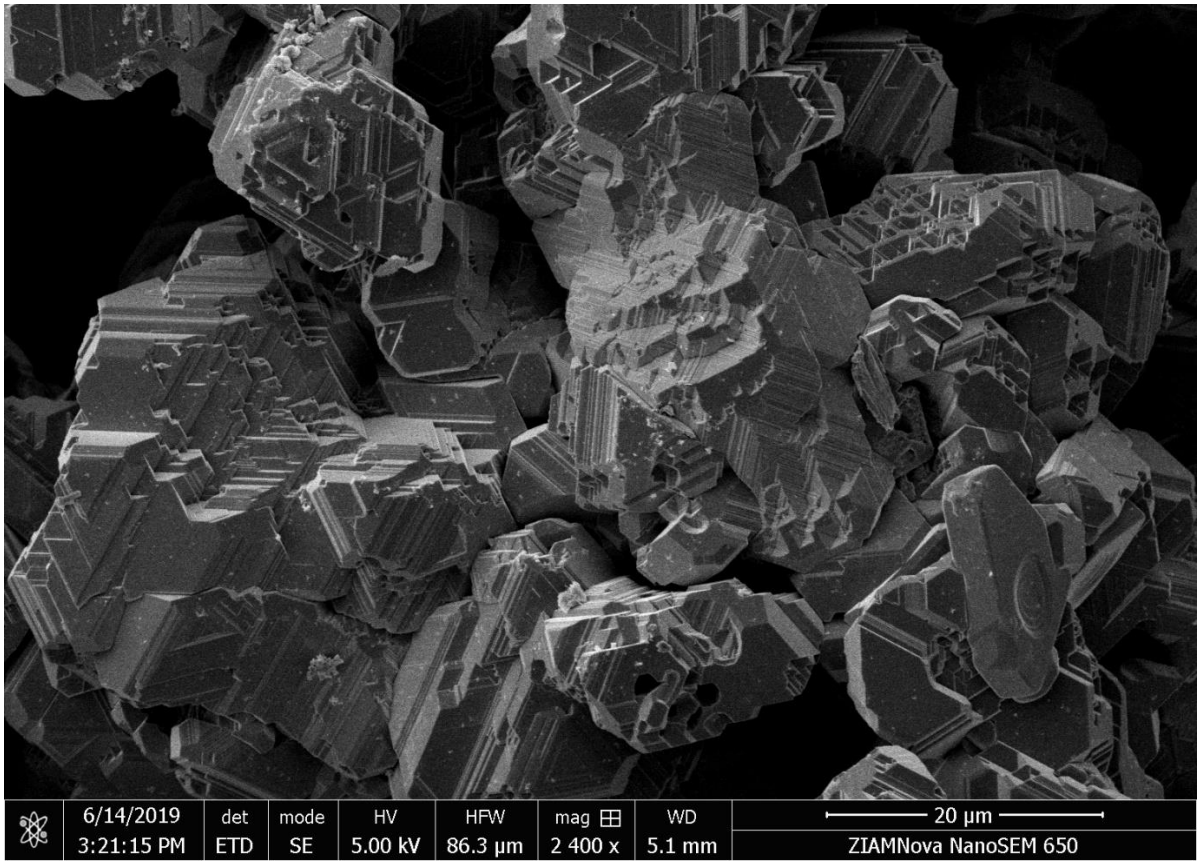


Figure 33: SEM image of polycrystals grown using  $\text{CaCl}_2$  flux (Sample 17b)

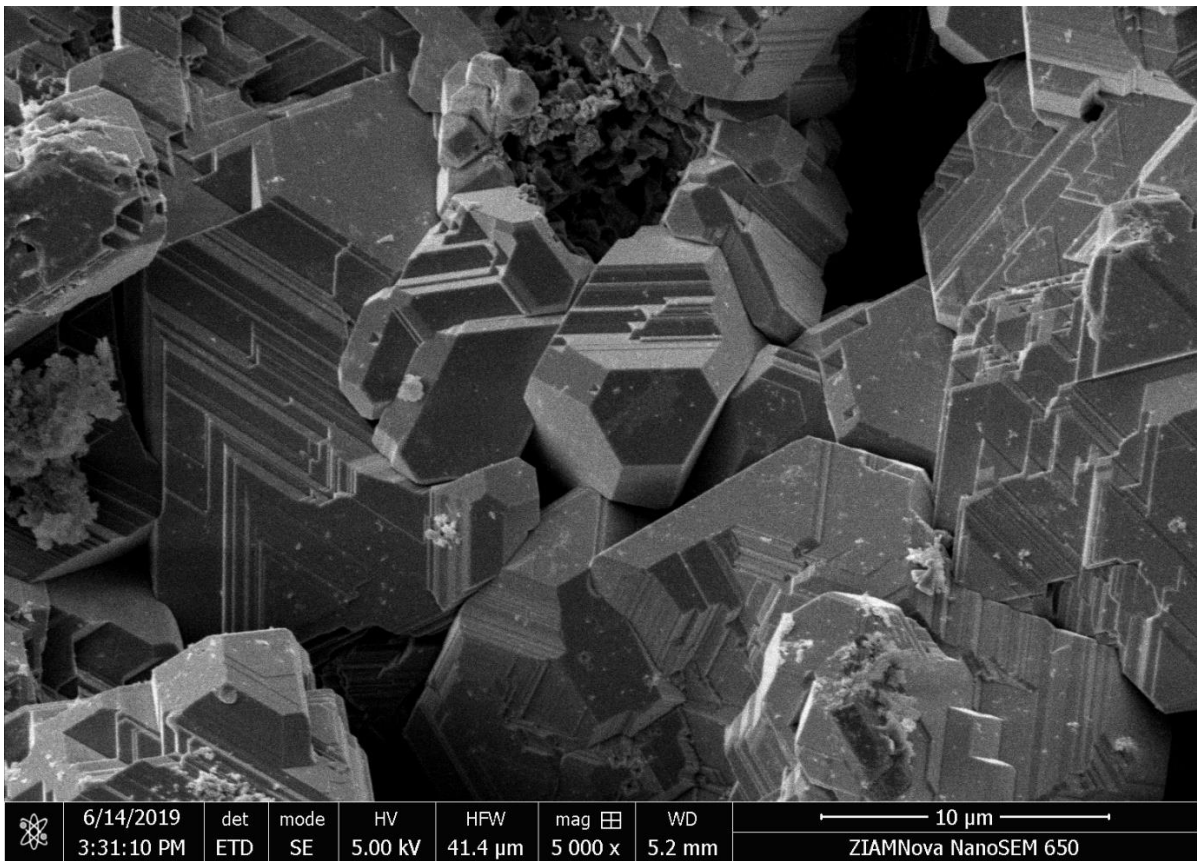


Figure 34: SEM image of polycrystals grown using  $\text{CaCl}_2$  flux (Sample 17b)

## 8. REFERENCES

- [1] S. Muhlbauer et al. (2009), "Skyrmion Lattice in a Chiral Magnet", *Science*, **323** (5916): 915-919.
- [2] A. Fert; V. Cros; J. Sampaio, (2013) "Skyrmions on the track". *Nature Nanotechnology*, **8** (3): 152–156,
- [3] S. Heinze et al. (2011), "Spontaneous atomic-scale magnetic skyrmion lattice in two dimensions", *Nature Physics*, **4** (9): 713-718.
- [4] I. Dzyaloshinskii (1958). "A thermodynamic theory of "weak" ferromagnetism of antiferromagnetics". *Journal of Physics and Chemistry of Solids*. **4** (4): 241.
- [5] P. Bak, & M.H. Jensen, (1980). "Theory of helical magnetic structures and phase transitions in MnSi and FeGe." *Journal of Physics C: Solid State Physics*, **13** (31): 881–885
- [6] S. Seki, M. Mochizuki, (2016) "Skyrmions in Magnetic Materials", *SpringerBriefs in Physics*.
- [7] T. Garel, & S. Doniach, (1982). "Phase transitions with spontaneous modulation-the dipolar Ising ferromagnet". *Physical Review B*, **26** (1): 325–329.
- [8] N. Nagaosa, Y. Tokura, (2013) "Topological properties and dynamics of magnetic skyrmions". *Nat. Nanotechnology*, **8** (12): 899-911.
- [9] T. Okuba, S. Chung, H. Kawamura, (2012) "Multiple  $q$ -States and the Skyrmion Lattice of the Triangular Lattice Heisenberg Antiferromagnet under Magnetic Fields", *Physical Review Letters*, **108**; (1), 1-5
- [10] J.E. Greedan, (2001) "Geometrically Frustrated Magnetic Materials", *J. Mater. Chem.*, **11** (1); 37-53.
- [11] J. Wosnitza, S.A. Zvyagin, & S. Zherlitsyn, (2016). "Frustrated magnets in high magnetic fields—selected examples". *Reports on Progress in Physics*, **79** (7); 074504.
- [12] L. Pauling, H.P. Klug, A.N. Winchell, (1935) "The structure of swedenborgite,  $\text{NaBe}_4\text{SbO}_7$ ." *American Mineralogist*, **20** (7); 492-501.
- [13] U.K. Rößler, A.A. Leonov, A.N. Bogdanov, (2010) "Skyrmionic textures in chiral magnets." *Journal of Physics: Conference Series* **200** (2); 022029
- [14] K. Kadowaki, K. Okuda, M. Date, (1982) "Magnetization and Magnetoresistance of MnSi. I." *J. Phys. Soc. Jpn.* **51**, 2433
- [15] M. Uchida, Y. Onose, Y. Matsui, Y. Tokura, (2006) "Real-space observation of helical spin order." *Science* **311** (5759); 359-361.
- [16] M. Valldor, (2004) "Syntheses and structures of compounds with  $\text{YBaCo}_4\text{O}_7$ – type structure" *Solid State Sciences* **6** (3), 251-266.
- [17] J.A. Hinkelbein, (1958) "Equilibrium in the reaction of barium with calcium chloride"
- [18] V. Petricek, M. Dusek, & L. Palatinus, (2014). "Crystallographic Computing System JANA2006: General features" *Z. Kristallogr.* **229** (5), 345-352.

- [19] L. Perier-Gamby & G. Thomas (1993) "Solid way synthesis of barium aluminate. Kinetic study of the formation of intermediate compounds" *Solid State Ionics* **63-65**, 128-135.
- [20] P. Süsse & M. Buerger (1970). "The structure of  $Ba_3(VO_4)_2$ ." *Zeitschrift Für Kristallographie - Crystalline Materials*, **131**(1-6).
- [21] E. Banks, M. Greenblatt, & B. Post (1970). "Crystal structures of synthetic spodiosites. Calcium chloride vanadate(V),  $Ca_2VO_4Cl$ , and calcium chloride arsenate,  $Ca_2AsO_4Cl$ ." *Inorganic Chemistry*, **9**(10), 2259-2264.
- [22] Roth, W. (1964). "The magnetic structure of  $Co_3O_4$ ." *Journal Of Physics And Chemistry Of Solids*, **25**(1), 1-10.
- [23] J. Reim, E. Rosén, W. Schweika, M. Meven, N. Leo, & D. Meier et al. (2014). "Structural invariance upon antiferromagnetic ordering in geometrically frustrated swedenborgite,  $CaBaCo_2Fe_2O_7$ ." *Journal Of Applied Crystallography*, **47**(6), 2038-2047.
- [24] L. He, C. Chen, N. Wang, W. Zhou, & L. Guo, (2007). "Finite size effect on Néel temperature with  $Co_3O_4$  nanoparticles." *Journal Of Applied Physics*, **102**(10), 103911.
- [25] A. Macdonald, P. Holdsworth, & R. Melko, (2011). "Classical topological order in kagome ice." *Journal Of Physics: Condensed Matter*, **23**(16), 164208.